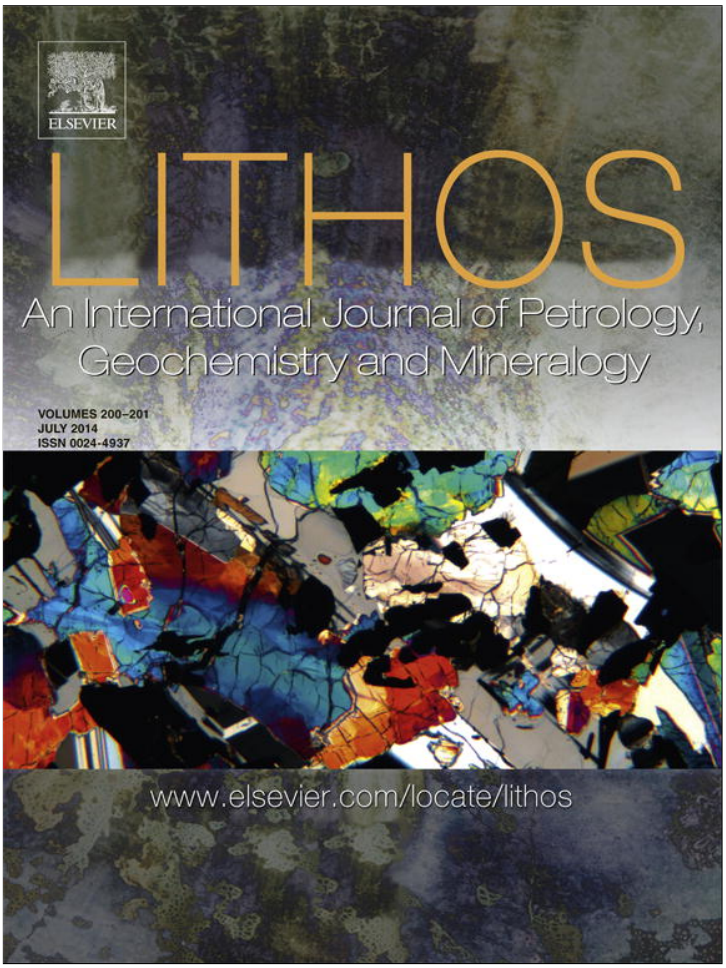

Lithos 200–201 (2014) 226–240

Contents lists available at ScienceDirect

Lithos

journal homepage: www.elsevier.com/locate/lithos

Petrological, geochemical and geochronological constraints on the origin of the Xiadong Ural–Alaskan type complex in NW China and tectonic implication for the evolution of southern Central Asian Orogenic Belt

Ben-Xun Su [a,b,c,*], Ke-Zhang Qin [a,**], Mei-Fu Zhou [b], Patrick Asamoah Sakyi [d], Joyashish Thakurta [e], Dong-Mei Tang [a], Ping-Ping Liu [a,b], Qing-Hua Xiao [a], He Sun [a]

[a] Key Laboratory of Mineral Resources, Institute of Geology and Geophysics, Chinese Academy of Sciences, P.O. Box 9825, Beijing 100029, China
[b] Department of Earth Sciences, University of Hong Kong, Hong Kong, China
[c] State Key Laboratory of Continental Dynamics, Northwest University, Xi'an 710069, China
[d] Department of Earth Science, University of Ghana, P.O. Box LG 58, Legon, Accra, Ghana
[e] Department of Geosciences, Western Michigan University, 1903 West Michigan Avenue, Kalamazoo, MI 49008, USA

ARTICLE INFO

Article history:
Received 23 January 2014
Accepted 4 May 2014
Available online 13 May 2014

Keywords:
Ural–Alaskan type complex
Central Asian Orogenic Belt
Mafic–ultramafic complex
Arc magmatism

ABSTRACT

The Xiadong mafic–ultramafic complex is located in the Central Tianshan Terrane, the southern part of the Central Asian Orogenic Belt. It is composed of dunite, hornblende clinopyroxenite, hornblendite and hornblende gabbro. Several dykes of hornblendite, hornblende gabbro and gabbroic diorite cut the main body. These rocks are characterized by adcumulate textures. The dunites contain high-Fo (92.3–96.6) olivines with rare orthopyroxene and plagioclase. Hornblende, chromite, and magnetite are common phases in all of the rock types. Geochemically, the rocks of the Xiadong complex display high MgO contents and extremely low trace element abundances. Although the rocks of the main body show higher MgO contents and lower trace element abundance compared to the dykes, both are characterized by flat REE patterns and enrichment of LILE relative to HSFE. These petrological, mineralogical and geochemical features indicate that the Xiadong complex is a typical Ural–Alaskan type complex. The cross-cutting and intrusive relationships of the rock units and their distinct geochemical features suggest that the main body represents a different pulse from the intrusive dyke. The positive whole-rock $\varepsilon_{Nd}(t)$ values, together with variable $(^{87}Sr/^{86}Sr)_i$ ratios, show a depleted mantle source metasomatized by subduction-related material. Zircon U–Pb dating on one hornblende gabbro from the main body of the complex yields a U–Pb $^{206}Pb/^{238}U$ age of 479 Ma, and zircons from three samples of the dykes yield ages of 477, 379 and 313 Ma. All the zircons have positive $\varepsilon_{Hf}(t)$ and slightly higher $\delta^{18}O$ than normal mantle, and their Hf–O isotopic values are correlated to their ages. The older samples are comparable to those from the Permian mafic–ultramafic complexes in the Beishan Terrane, which were derived from a mantle source metasomatized by subduction of the South Tianshan ocean, while the younger samples are similar to those from the Paleozoic complexes in the Eastern Tianshan, which record the subduction features of the Junggar ocean. These results suggest that the Central Tianshan was a continental arc from at least the Ordovician to the Carboniferous. The lithospheric mantle beneath the Central Tianshan was depleted in Sr–Nd–Hf isotopic compositions and was metasomatized by melts and/or fluids from the subduction of the South Tianshan and Junggar oceans in Paleozoic. The formation of the Xiadong Ural–Alaskan type complex was the product of arc magmatism via high-degree melting of the lithospheric mantle beneath the southern Central Asian Orogenic Belt.

1. Introduction

Ural–Alaskan type mafic–ultramafic complexes have been recognized as having a distinctive igneous tectonic setting, internal structure, composition and mineralization (Burg et al., 2009; Eyuboglu et al., 2010; Himmelberg and Loney, 1995; Irvine, 1974). These intrusions often occur at convergent plate margins and represent the products of arc magmas (Irvine, 1974; Taylor, 1967) or arc–root complexes (Brugmann et al., 1997; Debari and Coleman, 1989; Ishiwatari and Ichiyama, 2004). They are generally circular or elliptical in shape, having a dunite

* Correspondence to: B.-X. Su, Key Laboratory of Mineral Resources, Institute of Geology and Geophysics, Chinese Academy of Sciences, P.O. Box 9825, Beijing 100029, China. Tel.: +86 10 82998514.
** Corresponding author. Tel.: +86 10 82998183; fax: +86 10 62010846.
E-mail addresses: subenxun@mail.igcas.ac.cn (B.-X. Su), kzq@mail.igcas.ac.cn (K.-Z. Qin).

http://dx.doi.org/10.1016/j.lithos.2014.05.005
0024-4937/

core enveloped by successive concentric rims of wehrlite, olivine clinopyroxenite, hornblende clinopyroxenite, hornblendite and hornblende gabbro (Irvine, 1974; Johan, 2002). However, zoning can be discontinuous, incomplete or asymmetrical, as the complete sequence of lithologies is rarely observed in most complexes (Eyuboglu et al., 2010; Himmelberg and Loney, 1995). Mineralogically, most Ural–Alaskan type complexes are dominated by olivine, clinopyroxene, and hornblende with accessory chromite, ilmenite and magnetite, and with scarce orthopyroxene and plagioclase (Helmy and El Mahallawi, 2003; Himmelberg and Loney, 1995; Johan, 2002), although orthopyroxene and plagioclase are present in a few complexes, i.e. Karayaşmak complex in NE Turkey (Eyuboglu et al., 2010). They are interpreted as products of subduction-related arc magmas (Batanova et al., 2005; Burg et al., 2009; Eyuboglu et al., 2010; Himmelberg and Loney, 1995). Platinum group element mineralization is usually associated with Ural–Alaskan type complexes, whereas Ni–Cu mineralization is uncommon (Batanova et al., 2005; Hattori and Cabri, 1992; Johan, 2002). Although petrological and mineralogical features are widely accepted as identification criteria of most Ural–Alaskan type complexes, very little attention has been paid to their geochronology, which may shed more light on their emplacement mechanism and regional tectonic significance.

The Central Asian Orogenic Belt (CAOB) is the largest Phanerozoic juvenile orogenic belt in the world, and was formed in a complicated ocean–arc–microcontinent system by the subduction of the Paleo-Asian oceanic plate and multiple plate collisions, mainly in the Paleozoic (Fig. 1A; Jahn et al., 2000, 2004; Sengör et al., 1993; Sun et al., 2008; Windley et al., 2007; Xiao et al., 2004, 2009). The Chinese Tianshan occupies the southern margin of the CAOB and has been attributed to the northward subduction of the South Tianshan oceanic plate and subsequent southward subduction of the Junggar oceanic plate (Gao et al., 2006; Geng et al., 2009; Su et al., 2011a, 2012a, 2013a; Tang et al., 2010). One of the controversial issues regarding the long evolutionary history of the Tianshan Mountains lies in the duration of subduction and in the timing of the final closure of the Paleo-Asian ocean (Ao et al., 2010; Gao et al., 2009; Geng et al., 2011; Han et al., 2010; Qin et al., 2011; Su et al., 2011a, 2012a; Tang et al., 2012; Xiao et al., 2010). This controversy is partly due to the lack of typical rocks indicative of a particular tectonic environment or geologic event, such as Ural–Alaskan type complexes for an arc setting. Most of the Permian mafic–ultramafic complexes in the Eastern Tianshan and Beishan host Ni–Cu magmatic sulfide deposits, and have been interpreted as products of a post-orogenic extensional environment (Mao et al., 2008; Pirajno et al., 2008; Qin et al., 2011; Su et al., 2011a, b, 2012a, b, 2013a; Zhou et al., 2004). Our preliminary studies suggest that the Xiadong mafic–ultramafic complex in the Central Tianshan is petrologically and mineralogically similar to Ural–Alaskan type complex (Su et al., 2012c).

In this contribution, we report new major and trace element analyses, as well as whole-rock Sr–Nd and zircon U–Pb–Hf–O isotopic data, and combine these with previously published results of petrological and mineralogical studies of the Xiadong complex to provide further evidence that the Xiadong complex is a Ural–Alaskan type intrusion. Zircon U–Pb dating reveals an extremely long duration of magmatism

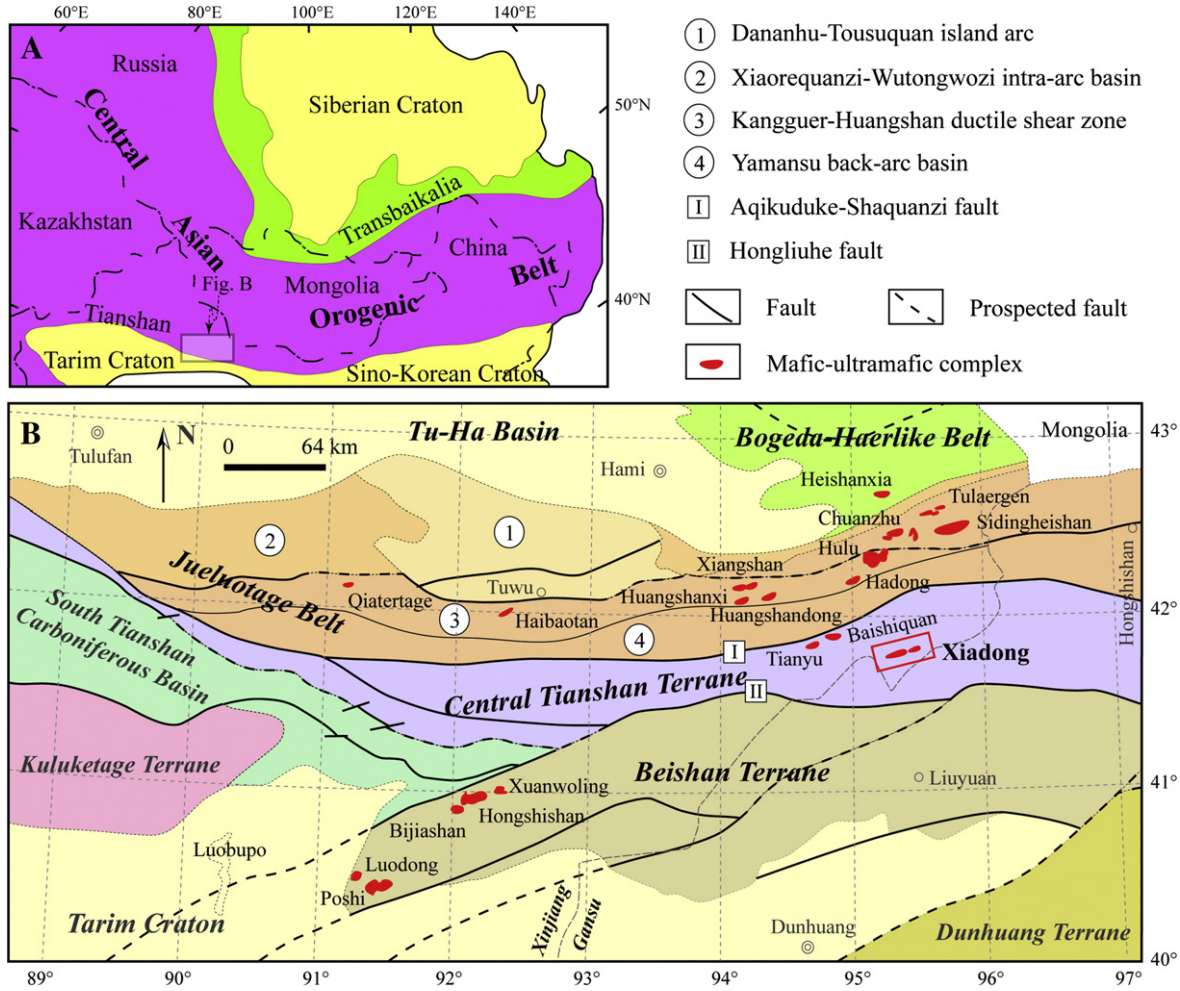

Fig. 1. (A) Location map of the study area in the Central Asian Orogenic Belt and portions of the Tarim Craton (modified after Jahn et al., 2000). (B) Regional geological map of the Eastern Tianshan and Beishan, showing the distribution of Paleozoic mafic–ultramafic complexes (modified after Su et al., 2011a). The Ural–Alaskan type Xiadong complex is located in the Central Tianshan.

in the construction of the Xiadong complex, which differs from other known Ural–Alaskan type complexes worldwide. The radiogenic and stable isotopes imply that the mantle source of the Xiadong complex was modified by two subduction events, which played critical roles in the evolution of the southern CAOB.

2. Regional geology

The CAOB, situated between the Siberian Craton to the north and the Tarim–Sino-Korean cratons to the south, was formed by the amalgamation and collision of a series of arcs (including fore-arcs, accretionary complexes and back-arc domains) and continental fragments (including both Gondwana- and Siberia-derived) (Fig. 1A; Hu et al., 2000; Jahn et al., 2000; Sengör et al., 1993; Sun et al., 2008; Windley et al., 2007; Xiao et al., 2009). The EW-trending Chinese Tianshan orogenic belt is located in the southern part of the CAOB (Fig. 1B). The eastern part of the Chinese Tianshan is referred to as the Eastern Tianshan in the literature. The Eastern Tianshan can be further divided into two sub-terranes: the Jueluotage Belt and the Central Tianshan, which are separated by the Aqikekuduke–Shaquanzi fault (Fig. 1B; BGMRXUAR, 1993; Xu et al., 2009).

The Jueluotage Belt has been subdivided, from north to south, into the Wutongwozi–Xiaorequanzi intra-arc basin, the Dananhu–Tousuquan island arc, the Kangguer–Huangshan ductile shear zone and the Yamansu back-arc basin (Fig. 1B; Qin et al., 2002). In this belt, there are abundant Paleozoic volcanic and sedimentary strata, including subaerial volcanics, sandstones and pelitic slates with inter-layered limestones, mudstones, siltstones and conglomerates (BGMRXUAR, 1993). Carboniferous–Permian magmatism was active, and resulted in the emplacement of Cu- and Au-rich, high-potassium, relatively oxidized, calc-alkaline to alkali magmas (Qin et al., 2002, 2003; Xu et al., 2009; Zhang et al., 2008). Abundant Early Permian mafic–ultramafic complexes are largely distributed along deep fractures in the Kangguer–Huangshan ductile shear zone (Fig. 1B), and contain significant magmatic Ni–Cu sulfide deposits (Han et al., 2010; Pirajno et al., 2008; Su et al., 2012a, d, 2013b).

The Central Tianshan Terrane consists of Precambrian crystalline basement overlain by Paleozoic sedimentary and volcanic strata, which also dominate the Beishan Terrane to the south (BGMRXUAR, 1993). The basement is composed mainly of the Mesoproterozoic Xingxingxia and Kawabulak formations (BGMRXUAR, 1993; Qin et al., 2002; Xu et al., 2009). Permian mafic–ultramafic complexes, such as the 280 Ma Tianyu (Qin et al., 2011), 285 Ma Baishiquan (Su et al., 2011a) and other mafic bodies, are distributed along the northern margin of the Central Tianshan Terrane (Fig. 1B). The rock types present in the intrusions are mainly peridotite, olivine pyroxenite, gabbro and diorite, and all of the rocks contain phlogopite and hornblende. Both peridotite and olivine pyroxenite are the host rocks of the Ni–Cu sulfide ores (Chai et al., 2008; Song et al., 2011; Tang et al., 2011, 2012). The Xiadong mafic–ultramafic complex is located in the center of the Central Tianshan Terrane, and shows distinct petrological and mineralogical features relative to the other intrusions.

The Xiadong mafic–ultramafic complex is elongated E–W and covers an area of 7 km in length and a maximum of 0.5 km in width (Fig. 2). It intrudes Neoproterozoic schist, gneiss, and marble (Xu et al., 2009). The field relations between the rock units are mainly observed in prospect pits (Fig. 3A). The main body of the complex is composed of dunite, hornblende clinopyroxenite, hornblendite and hornblende gabbro, and these are cut by many dykes including hornblendite, hornblende gabbro and gabbroic diorite (Fig. 2). All outcrops are aligned in an E–W direction parallel to the direction of elongation of the complex (Fig. 2). The rock units within the Xiadong complex display intrusive contacts. In the lateral A–B profile, many hornblendite and hornblende gabbro dykes occur within the dunite (Fig. 2). There are two types of dunites: one is dark green and the other is light yellow, and chilled margins are observed in the contacts between the two (Fig. 3B). Small-scale rhythmic layering of olivine and chromite occurs in some dunites (Fig. 3C; Su et al., 2012c; Sun et al., 2009). Cross-cutting relations are also observed between hornblendite and hornblende clinopyroxenite (Fig. 3D), both of which show a cumulate texture (Fig. 3E; Su et al., 2012c). The hornblende clinopyroxenite unit is only in the form of a dyke, with very local extension with no contact relation with the dunite.

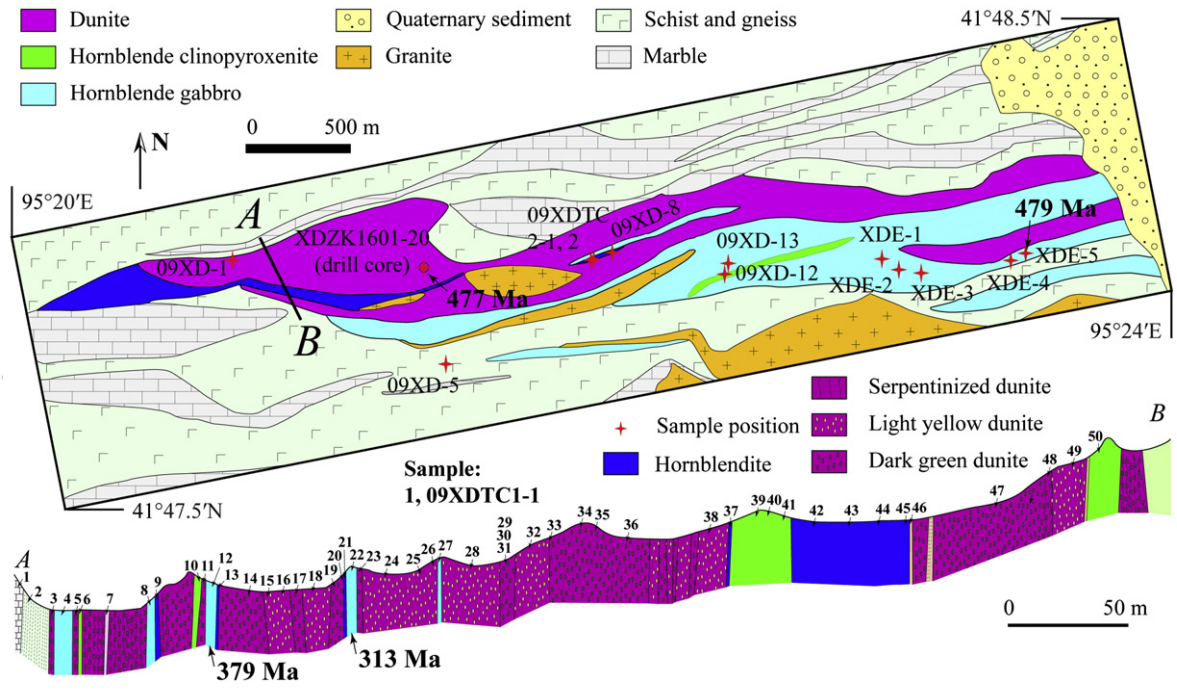

Fig. 2. Geological map and lateral A–B profile of the Xiadong mafic–ultramafic complex, showing its sampling positions, as well as the major rock units of dunite, hornblende clinopyroxenite, hornblendite and hornblende gabbro. Note that some lithological units are composites in this scale.

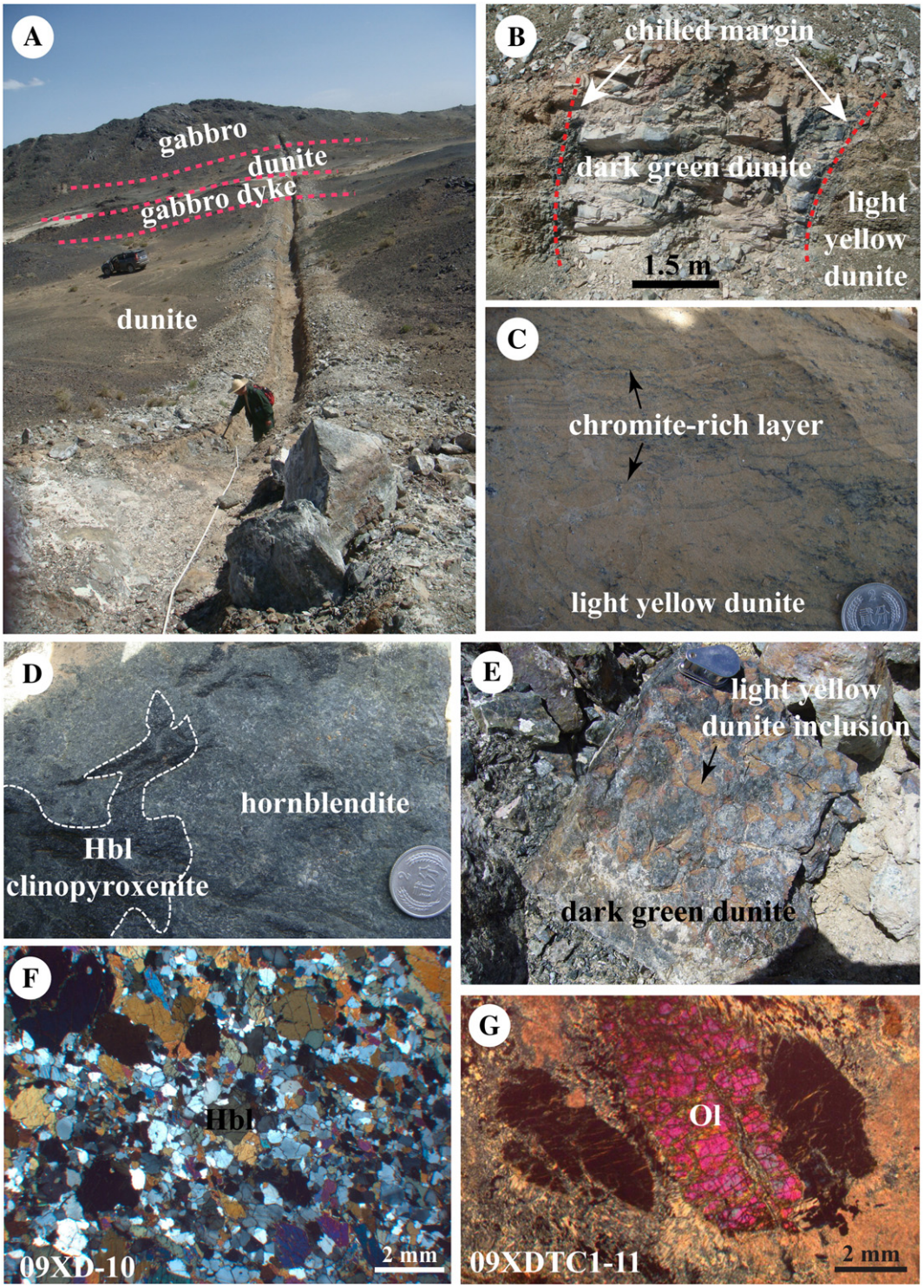

Fig. 3. Field outcrop and petrological photographs of the Xiadong mafic–ultramafic complex: (A) the hornblende gabbro occurring as a dyke in the dunite; (B) chilled margins present in the contact between light yellow and dark green dunites; (C) partly bent chromite-rich layer in the light yellow dunite; (D) intrusive relation between hornblendite and hornblende clinopyroxenite; (E) coarse-grained light yellow olivine (Ol) inclusions in dark green dunite; (F) adcumulate texture in the hornblendite; and (G) cross polarized image showing fresh olivine inclusion in serpentinized host dark green dunite.Figures A, B and D are from Su et al. (2012c).

Additionally, the light yellow dunites are occasionally present as inclusions in the dark green dunite (Fig. 3E).

3. Petrology of the Xiadong mafic–ultramafic complex

Generally, the rocks of the Xiadong complex are fresh and only show a small amount of secondary alteration. Late-stage deformation and metamorphism might have occurred in the complex, as evidenced by partly bent chromite-rich layers (Fig. 3C), strongly deformed structures in hornblende clinopyroxenite and metamorphic features in hornblende gabbro described below. The rocks from the main body and the dykes of the Xiadong complex share common aspects in their petrography and mineralogy, but are distinct in geochemistry and age. Thus, we discuss the petrological and mineralogical aspects of rocks

from the main body and dykes together; and their geochemical compositions separately in the following sections.

3.1. Dunite

Both light yellow and dark green dunites are made up of olivine (85–95% in volume) and chromite (5–15%) with accessory hornblende and clinopyroxene (<1–2%), and exhibit an adcumulate texture. The light yellow dunites are fresh with only minor alteration of clinopyroxene, whereas the dark green dunites have been strongly serpentinized with most olivine being altered to serpentine, and clinopyroxene being replaced by actinolite or tremolite. Olivine in both types of dunites is of variable size, ranging from <0.5 mm to 5 mm in diameter. Compositionally, forsterite (Fo) contents range from 92.3 to 96.6, MnO from 0.03 wt.% to 0.23 wt.%, and NiO from 0.05 wt.% to 0.76 wt.%, with extremely low CaO of <0.04 wt.% (Su et al., 2012c; Sun et al., 2009). The olivine inclusions in the strongly serpentinized dark green dunites (Fig. 3G) show similar compositions to those in the fresh light yellow dunites. Although large compositional variations in olivine are present in these dunites, the olivine in individual samples is chemically homogeneous.

Chromites occur as interstitial grains or as rhythmic layers, and most often display elongated crystal shapes, although some are rounded. They have low Al_2O_3 (<12.0 wt.%), TiO_2 (<0.70 wt.%) and MgO (<7.00 wt.%) contents, and large variations with overall high contents of Cr_2O_3 (up to 43.9 wt.%) and FeO (65–96 wt.%), with low Mg# ($100 \times Mg/(Mg + Fe)$) values (<10.0) and very high Cr# ($100 \times Cr/(Cr + Al)$) values (95–100) (Su et al., 2012c). These chromites are thus compositionally subordinate to Fe-rich chromite and Cr-rich magnetite. Most clinopyroxenes are strongly fractured and are altered to actinolite, tremolite or chlorite. Yellowish brown hornblende commonly forms irregular patches surrounding olivine and clinopyroxene.

3.2. Hornblende clinopyroxenite

The hornblende clinopyroxenite is composed of clinopyroxene, hornblende, and accessory magnetite and chromite. Intra-crystalline deformation is developed in mineral grains. Cumulus clinopyroxenes are mostly metamorphosed to actinolite or tremolite, preserving a clinopyroxene core with hornblende rims. The clinopyroxene is diopsidic and rich in CaO (24.6–25.7 wt.%). Clinopyroxene in hornblende clinopyroxenite shows relatively low SiO_2 (~50.5 wt.%) and Mg# (85–89), and high TiO_2 (0.28–1.22 wt.%) and Al_2O_3 (2.97–6.42 wt.%). Hornblende in the hornblende clinopyroxenite is generally rich in MgO and poor in alkaline components, and is classified as magnesio-hornblende and tremolite (Su et al., 2012c). The hornblendes are interstitial and commonly altered to actinolite along their rims. Magnetite and chromite grains are usually less than 40 μm in diameter.

3.3. Hornblendite

The hornblendite contains mainly hornblende and accessory minerals including plagioclase, magnetite, ilmenite, titanite and chromite. Hornblende crystals are cumulate and mostly <0.5 mm in size, although some are 2–4 mm in diameter and display recrystallized textures with fine-grained hornblende at their margins. Primary hornblende is mainly pargasite and secondary hornblende is magnesio-hornblende and tremolite. The primary hornblende has high contents of TiO_2, Al_2O_3, FeO and Na_2O, and low SiO_2 and MgO contents with variable Mg# of 74–96 (Su et al., 2012c; Sun et al., 2009). Plagioclase crystals are fine-grained (<1 mm in size) and have modal abundance of 5–15%. Plagioclase is commonly altered to zoisite. Accessory minerals occur as interstitial grains and are generally less than 0.4 mm in size. Titanite commonly occurs as rims around ilmenite.

3.4. Hornblende gabbro

The hornblende gabbro consists of plagioclase, clinopyroxene, hornblende, magnetite, ilmenite, titanite and apatite. It has an equigranular texture and mineral grains are <1.5 mm in diameter. Plagioclase crystals are commonly zoisitized and have Si–Al–Na depletion, with anorthite (An) values of 9.72–30.9 (Su et al., 2012c). Clinopyroxene and hornblende are altered to actinolite or tremolite, and contain ilmenite lamellae. Clinopyroxene has a variable content of SiO_2 (51.3–55.7 wt.%), low contents of TiO_2 (0–0.16 wt.%), Al_2O_3 (0.49–2.98 wt.%), FeO (0.51–1.29 wt.%) and Na_2O (0.03–0.33 wt.%), and extremely high Mg# (95.8–98.4) (Su et al., 2012c). Primary hornblende in the hornblende gabbros is mainly magnesio-hornblende with a relatively homogeneous composition, whereas secondary minerals formed after clinopyroxenes are rich in MgO and poor in Na_2O. High-Mg features in silicate minerals can be attributed to crystallization of magnetite and ilmentite which host large amount of Fe. The modal abundance of magnetite and ilmenite in the hornblende gabbros can reach up to 15%. Magnetite, in most cases, displays parallel intergrowth with ilmenite, and locally occurs as interstitial grains.

4. Analytical methods

4.1. Zircon U–Pb dating and Hf–O isotopes

Zircon grains were separated using standard density and magnetic separation techniques, and together with zircon standards TEMORA and 91500, were mounted in epoxy resin and then polished to expose the crystal centers. All zircons were photographed in transmitted and reflected light, as well as with cathodoluminescence (CL) to reveal their internal structures. The mount was vacuum-coated with high-purity gold prior to U–Pb and O isotopic analyses.

Measurements of U, Th and Pb isotopes were conducted using a Cameca IMS 1280 large-radius SIMS in the Institute of Geology and Geophysics, Chinese Academy of Sciences, Beijing. Analytical procedures are the same as those described by Li et al. (2009, 2010). The O_2^- primary ion beam was accelerated to 13 kV, with an intensity of ca. 8 nA. The ellipsoidal spot was approximately 20 × 30 μm in size. Oxygen flooding (e.g., Whitehouse et al., 1999) was used to increase the O_2 pressure to ca. 5×10^{-6} Torr in the sample chamber, enhancing Pb+ sensitivity by a factor of >2 to a value of 24–28 cps/nA/ppm for zircon. Precise mass calibration was maintained by using an automatic routine in the Cameca CIPS software to scan over large peaks and extrapolate the mass to B-field curve for peaks between these reference points (Whitehouse and Kamber, 2005). Correction of common lead was made using measured ^{204}Pb. An average Pb of present-day crustal composition (Stacey and Kramers, 1975) was used for common Pb, assuming that it is largely due to surface contamination introduced during sample preparation. Data reduction was carried out using the Isoplot/Ex rev. 2.49 Program (Ludwig, 2001).

Zircon oxygen isotopes were measured using the same Cameca IMS 1280 SIMS. The Cs+ primary ion beam was accelerated at 10 kV, with an intensity of ca. 2 nA and rastered over a 10 μm area producing a spot of about 20 μm in diameter (10 μm beam diameter + 10 μm raster). Oxygen isotopes were measured in multi-collector mode using two off-axis Faraday cups. Uncertainties on individual analyses are reported at the 1σ level. With low noise on the two FC amplifiers, the internal precision of a single analysis was generally better than 0.2‰ for the $^{18}O/^{16}O$ ratio. Values of $\delta^{18}O$ were standardized to VSMOW (Vienna Standard Mean Ocean Water) and reported in standard per mil notation. The instrumental mass fractionation factor was corrected using the 91500 zircon standard with $(\delta^{18}O)_{VSMOW} = 9.9‰$ (Wiedenbeck et al., 2004). Detailed working conditions and analytical procedures have been described by Li et al. (2010).

In situ zircon Lu–Hf isotopic analyses were carried out on a Neptune multi-collector ICP-MS equipped with a Geolas-193 laser-ablation

system in the State Key Laboratory of Continental Dynamics, Northwest University, Xi'an. The Lu–Hf isotopic data were obtained from the same zircon grains that were previously analyzed for U–Pb and O isotopes, with ablation pits of 40–80 μm in diameter, ablation time of 26 s and repetition rate of 8 Hz. The detailed analytical procedures are described in Li et al. (2010) and Wu et al. (2006). Measured $^{176}Hf/^{177}Hf$ ratios were normalized to $^{179}Hf/^{177}Hf = 0.7325$.

4.2. Major and trace element analyses

Major elements were determined using a Shimadzu X-ray fluorescence spectrometer (XRF-1500) on fused glass beads. Analytical uncertainties were 1–3% for elements present in concentrations >1 wt.% and about 10 wt.% for elements present in concentrations <1.0 wt.%. Trace elements were determined by inductively coupled plasma mass spectrometry (ICP-MS), using an Agilent 7500a system after the digestion of the samples in a mixture of ultra-pure HF and HNO_3 in Teflon bombs. Measurement procedures are described in detail by Chu et al. (2009). Precision of the ICP-MS analyses was generally better than 5%. Major and trace elements were measured in the Institute of Geology and Geophysics, Chinese Academy of Sciences.

4.3. Sr–Nd isotopic analyses

About 100–150 mg of whole rock powder was completely decomposed in a mixture of HF–$HClO_4$ for Sr–Nd isotopic analysis. Sr and REE were separated in quartz columns with a 2 ml resin bed of AG 50W-X12, 200–400 mesh. Nd was separated from other REEs in quartz columns using 0.7 ml P507-coated Teflon powder as the extraction resin. Procedural blanks were <200 pg for Sr and <50 pg for Nd. For the measurements of isotopic composition, Sr was loaded with a Ta–HF activator on a single W filament and Nd was loaded as phosphate, and measured in a Re-double-filament configuration. $^{143}Nd/^{144}Nd$ ratios were normalized to $^{146}Nd/^{144}Nd = 0.7219$ and $^{87}Sr/^{86}Sr$ ratios to $^{86}Sr/^{88}Sr = 0.1194$. Isotopic ratios were measured on a VG-354 thermal ionization magnetic sector mass spectrometer in the Laboratory for Radiogenic Isotope Geochemistry, Institute of Geology and Geophysics, Chinese Academy of Sciences, Beijing. The chemical separation and isotopic measurement procedures followed that of Zhang et al. (2001). Mass fractionation corrections for Sr and Nd isotopic ratios were based on values of $^{86}Sr/^{88}Sr = 0.1194$ and $^{146}Nd/^{144}Nd = 0.7219$. Uncertainties in Rb/Sr and Sm/Nd ratios were less than 2% and 0.5%, respectively.

5. Results

5.1. Zircon morphology, U–Pb ages and Hf–O isotopes

Four hornblende gabbro samples were selected for zircon U–Pb dating and in situ Hf–O isotopic analyses. Samples 09XDTC1-12 and 09XDTC1-22 were collected from hornblende gabbro dykes that intrude the dunite bodies (Fig. 2). Sample 09XDTC1-12 consists of fresh fine-grained plagioclase, clinopyroxene and hornblende with accessory ilmenite (Fig. 4A). Sample 09XDTC1-22 is fine-grained and exhibits cumulate texture, with a mineral assemblage of plagioclase, clinopyroxene, and hornblende, with accessory ilmenite; some clinopyroxene grains are partly altered to actinolite (Fig. 4B, D; Su et al., 2012c). Sample XDZK1601-20 was obtained from a drill core (Fig. 2), displays a cumulate texture and is composed of plagioclase, clinopyroxene and hornblende with minor ilmenite (Fig. 4C). Sample XDE-5 represents the hornblende gabbro of the main body, and consists of green zoisite observed in hand specimen (Fig. 4E) and actinolitized clinopyroxene in back-scattered image (Fig. 4F).

5.1.1. Sample 09XDTC1-12: hornblende gabbro dyke

Zircons separated from sample 09XDTC1-12 are generally equant to short prismatic, colorless and transparent. The lengths of these crystals range from 30 to 60 μm, with aspect ratios of 1:1 to 1.5:1. They have rounded terminations and display only weak oscillatory or patchy zoning with low luminescence (Fig. 5A). The zircons have U, Th and Pb contents of 68–236 ppm, 30–188 ppm, and 5–17 ppm, respectively, with Th/U ratios in the range of 0.44–0.80 (Table 1S). All analyses are concordant, yielding a concordia $^{206}Pb/^{238}U$ age of 379 ± 5 Ma (MSWD = 0.01) (Fig. 6). The zircons have homogeneous Hf and O isotopic compositions: $^{176}Hf/^{177}Hf$ ranges from 0.282803 to 0.282898, corresponding to $\varepsilon_{Hf}(t) = +9.44$ to $+12.80$, and $\delta^{18}O$ in the range of +5.71‰ to +7.02‰ (Table 2S). The $\delta^{18}O$ values of the zircons from sample 09XDTC1-12 are thus higher than the value of +5.3 ± 0.3‰ for normal mantle zircons (Valley et al., 1998).

5.1.2. Sample 09XDTC1-22: hornblende gabbro dyke

Zircons from sample 09XDTC1-22 are prismatic, colorless and transparent. Most grains are subhedral, and some occur as fragments. Crystal lengths range from 40 to 100 μm, with aspect ratios of 1:1 to 2:1. In CL images, most zircons have concentric zoning, and a few grains show weakly oscillatory or patchy zonation with moderate brightness (Fig. 5B). These zircons have U, Th and Pb values from 62 to 184 ppm, from 35 to 172 ppm and from 4 to 12 ppm, respectively, with Th/U ratios ranging from 0.56 to 1.00 (Table 1S). All the analyses yielded concordant U–Pb ages, defining a concordia age of 313 ± 3 Ma (MSWD = 1.3) (Fig. 6). The zircons display homogeneous Hf and O isotopic compositions: $^{176}Hf/^{177}Hf$ ranges from 0.282904 to 0.282964, corresponding to $\varepsilon_{Hf}(t) = +11.55$ to $+13.67$, and $\delta^{18}O$ in the range of +4.57‰ to +6.23‰ (Table 2S), which are mostly consistent with the $\delta^{18}O$ value of 5.3 ± 0.3‰ for normal mantle zircons (Valley et al., 1998).

5.1.3. Sample XDZK1601-20: hornblende gabbro dyke

Sample XDZK1601-20 has large zircons, most of which are present as fragments that have variable lengths, ranging from 80 to 200 μm with aspect ratios of 1:1 to 4:1. They have concentric and oscillatory zoning although a few grains show patchy zoning (Fig. 5C). The SIMS analytical results show that the U, Th and Pb contents of these zircons are high, in ranges of 159–413 ppm, 89–378 ppm and 15–43 ppm respectively, with Th/U ratios of 0.49–0.92 (Table 1S). All analyses have concordant U–Pb ages and define a concordia $^{206}Pb/^{238}U$ age of 477 ± 4 Ma (MSWD = 1.13) (Fig. 6). The zircons have $^{176}Hf/^{177}Hf$ ratios ranging from 0.282548 to 0.282860, corresponding to $\varepsilon_{Hf}(t)$ of +2.57 to +6.53, and $\delta^{18}O$ values of +5.01‰ to +7.43‰ (Table 2S).

5.1.4. Sample XDE-5: hornblende gabbro

Zircons from sample XDE-5 vary from euhedral to anhedral, and range from equant to short or long prismatic (Fig. 5D). The lengths of the crystals range from 40 to 110 μm with aspect ratios from 1:1 to 4:1. The CL images show that most crystals display oscillatory or patchy linear zoning with variable luminescence, although some grains have dark cores enveloped by thinly-zoned growth rims (Fig. 5D). These zircons have large variations in U (100–371 ppm), Th (60–316 ppm) and Pb (16–159 ppm) contents, with Th/U ratios of 0.28–0.85 (Table 1S). The zircons yield scattered U–Pb ages that are concordant and plot along the concordia line. $^{206}Pb/^{238}U$ ages of these zircons are in the range of 402 Ma–2075 Ma. Seven analyses yield a concordia age of 479 Ma (Fig. 6D), which represents the crystallization age of the sample, whereas the younger zircons are probably modified by late-stage metamorphism or Pb loss and the older grains were inherited from the country rocks. The ~479 Ma zircons have $^{176}Hf/^{177}Hf$ ratios ranging from 0.282366 to 0.282625, corresponding to $\varepsilon_{Hf}(t)$ values of +2.59 to +5.01, and $\delta^{18}O$ ranging from +2.35‰ to +9.79‰, whereas other zircons show rather large Hf and O isotopic variations (Table 2S).

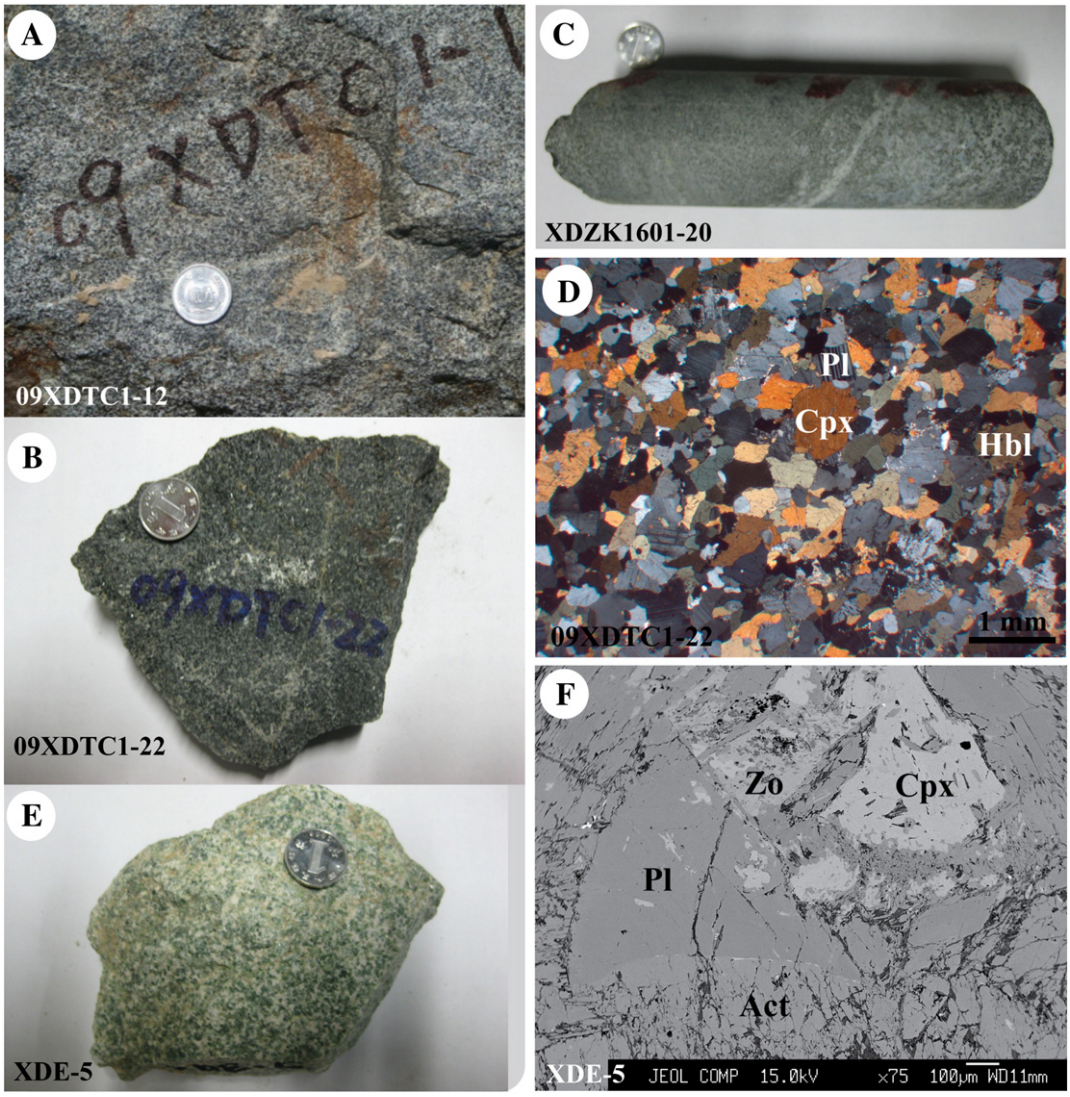

Fig. 4. Petrophotographs of four hornblende gabbro samples for zircon U–Pb dating. (A) 09XDTC1-12 consists of fresh fine-grained plagioclase (Pl), clinopyroxene (Cpx) and hornblende with accessory ilmenite; (B) and (D) sample 09XDTC1-22 exhibits cumulate and fine-grained texture with mineral assemblage of plagioclase, clinopyroxene, and hornblende with accessory ilmenite, with some clinopyroxene grains partly metamorphosed to actinolite (Act); (C) sample XDZK1601-20 collected from a drill bore; (E) and (F) sample XDE-5 shows metamorphosed characteristics such as zoisite (Zo) observed in hand specimen and actinolitized clinopyroxene in the back-scattered image.

5.2. Major and trace elements

The light yellow and dark green dunites have nearly identical geochemical compositions. All the dunites except sample 09XDTC1-38 have extremely refractory compositions, with low Al_2O_3 (0.38–1.81 wt.%) and CaO (0.11–0.96 wt.%) contents and high MgO (37.3–43.8 wt.%) contents and Mg# (Mg# = 100 × Mg/(Mg + Fe); 90.1–92.7) (Table 3S; Fig. 7). They display large variations in Ni and Cr abundances, ranging from 1320 to 1987 ppm and from 2003 to 7063 ppm, respectively (Table 3S). They are strongly depleted in rare earth elements (REEs) and other incompatible elements relative to primitive mantle values (Table 3S; Fig. 8).

Hornblende clinopyroxenites are distinguished from the dunites by having much higher Al_2O_3 (3.78–7.97 wt.%) and CaO (6.94–17.0 wt.%), significantly lower Ni (256–289 ppm) and Co (43–81 ppm), and slightly more enrichment in incompatible trace elements (Table 3S; Figs. 7, 8).

Hornblendites have MgO contents of 8.5–14.0 wt.%, Al_2O_3 of 10.7–19.4 wt.%, FeO_T (total Fe) of 3.2–18.6 wt.% and CaO of 10.0–14.7 wt.% (Table 3S). The hornblendites from the main body display higher Al_2O_3 and CaO and lower FeO_T than those hornblendite dykes (Fig. 7). The two types of hornblendite also show different REE concentrations and Eu anomaly in their REE patterns (Table 3S; Fig. 8).

The hornblende gabbros from the main body have similar Mg# values, higher Al_2O_3, CaO and $Na_2O + K_2O$, lower FeO_T and slightly higher incompatible trace element abundances compared to the dunite and hornblende clinopyroxenite. The hornblende gabbro dykes have relatively lower Al_2O_3 and CaO, higher FeO_T, $Na_2O + K_2O$ and trace elements than those from the main body (Table 3S; Figs. 7, 8). One gabbroic diorite sample resembles the hornblende gabbro dykes in most geochemical signatures.

Overall, the rocks from the main body and intrusive dykes show distinct correlations in major oxides, especially in the plots of FeO_T vs. MgO, CaO vs. MgO and $Na_2O + K_2O$ vs. MgO (Fig. 7). In terms of trace elements, the intrusive dykes have higher trace element abundances and have distinctive Eu, Rb, Zr, Hf and Ti anomalies relative to the rocks from the main body, although they share many geochemical similarities, such as flat REE patterns and large ion lithophile element (LILE) enrichment relative to high field strength element (HFSE) (Fig. 8).

The granite and biotite–quartz schist, which are the country rocks of the Xiadong complex, have high SiO_2 (75.2 wt.% and 64.8 wt.%), Al_2O_3

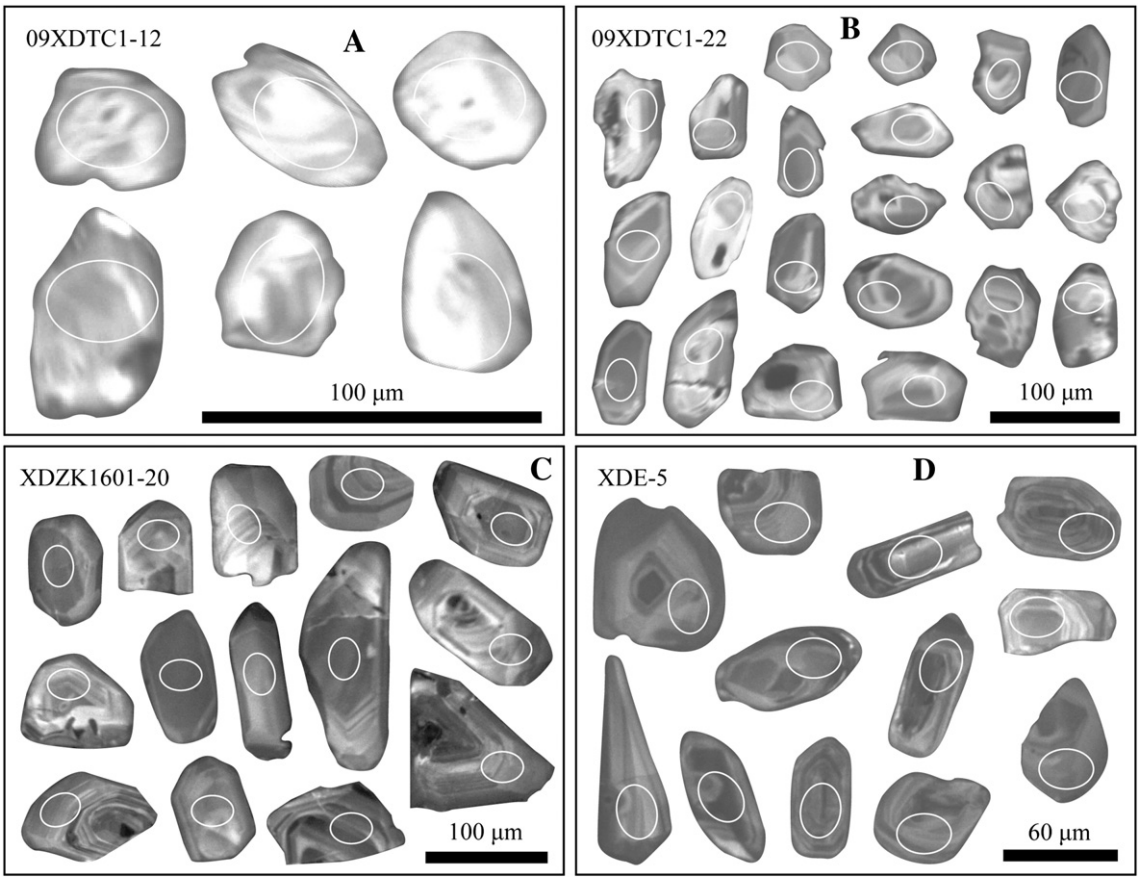

Fig. 5. Cathodoluminescence images of representative zircons from four hornblende gabbros from the Xiadong mafic–ultramafic complex. The ellipses indicate the analyzing spots for U–Pb and O–Hf isotopes.

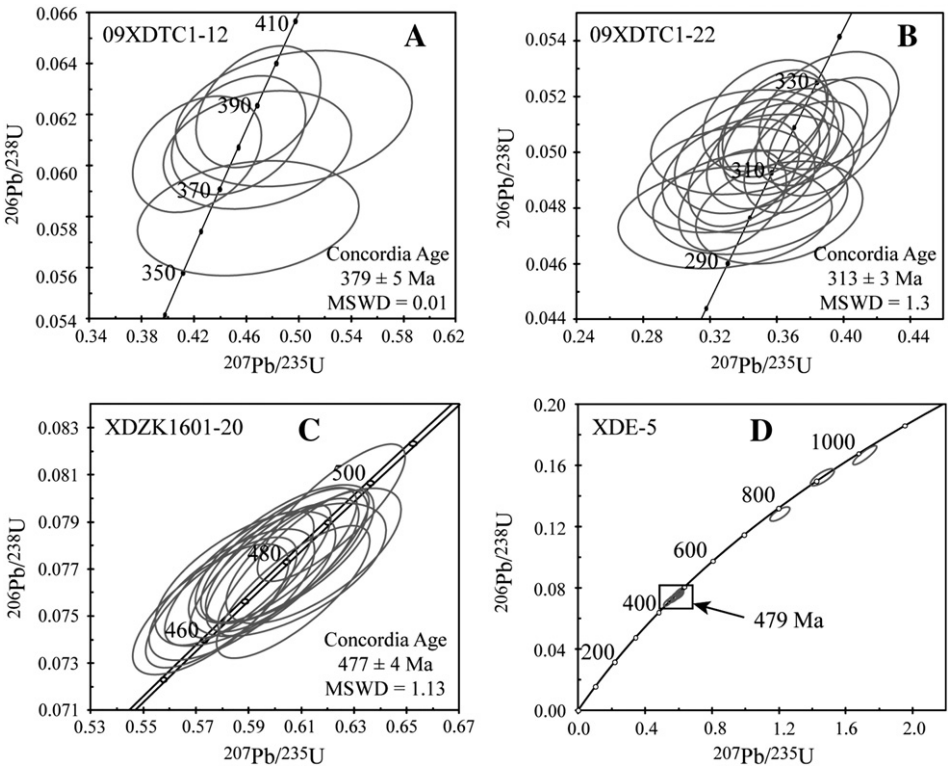

Fig. 6. U–Pb concordia plots (2σ error) of zircons from four hornblende gabbros of the Xiadong mafic–ultramafic complex.

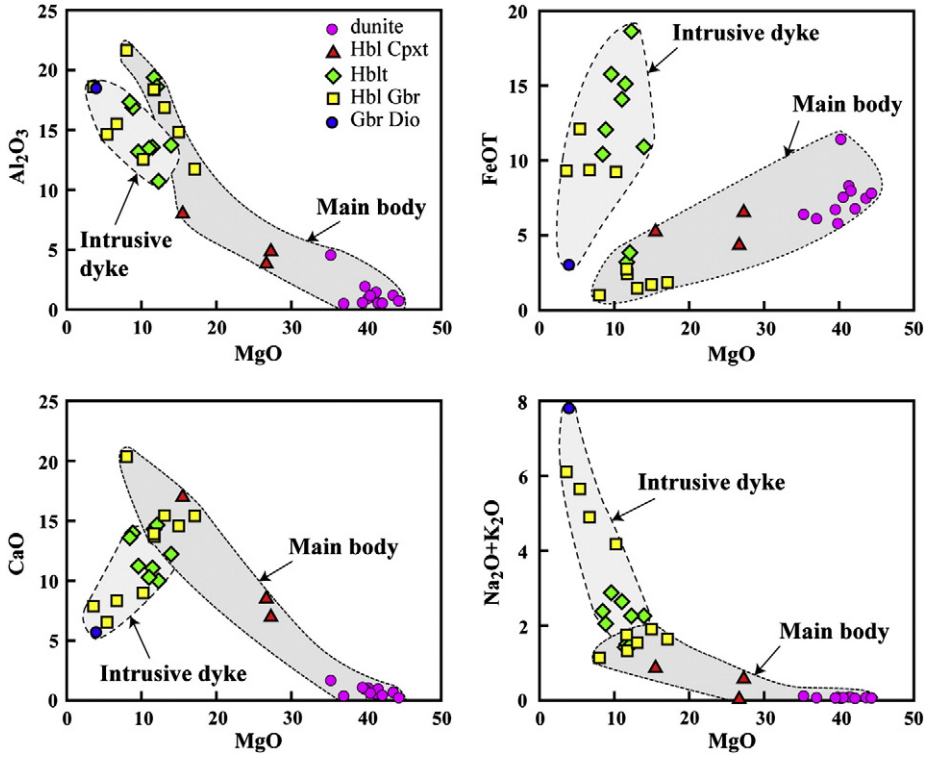

Fig. 7. Diagrams of MgO versus Al_2O_3, FeO_T (total Fe), CaO, and $Na_2O + K_2O$ of the investigated rocks from the Xiadong mafic–ultramafic complex. Hbl Cpxt, hornblende clinopyroxenite; Hblt, hornblendite; Hbl Gbr, hornblende gabbro; Gbr Dio, gabbro diorite.

(14.4 wt.% and 17.1 wt.%) and Na_2O (5.21 wt.% and 5.00 wt.%) contents, and display trace element enrichment and patterns that are distinct from the intruded mafic–ultramafic rocks (Table 3S; Fig. 8).

5.3. Sr–Nd isotopes

According to field observation and zircon U–Pb dating results, we deduce ages of 480 Ma for the formation of the hornblende gabbro and hornblende clinopyroxenite of the main body, and 380 Ma and 313 Ma for the hornblende gabbro dykes. These ages have then been used re-calculate the initial Sr–Nd isotopic ratios of the corresponding rocks. The Xiadong mafic–ultramafic rocks show large Sr–Nd isotopic variations. Their $(^{87}Sr/^{86}Sr)_i$ ratios vary from 0.703882 to 0.710486, and the $(^{143}Nd/^{144}Nd)_i$ ratios are in the range of 0.512041–0.512565, which correspond to $\varepsilon_{Nd}(t)$ of 0.29–8.18 (Table 1; Fig. 9).

6. Discussion

6.1. Geochemical constraints on Ural–Alaskan type Xiadong complex

Ural–Alaskan type complexes are distinguished from other mafic–ultramafic intrusions mainly on the basis of petrographic and mineralogical characteristics. The former are typically composed of dunite, wehrlite, olivine clinopyroxenite, hornblende clinopyroxenite, hornblendite and hornblende gabbro (Himmelberg and Loney, 1995; Irvine, 1974; Johan, 2002). They display distinctive mineral assemblages and compositions, and are characterized by the absence of orthopyroxene and plagioclase in the ultramafic rocks, the presence of hornblende in all rock types, and cumulative clinopyroxene consistent with an arc setting (Eyuboglu et al., 2010; Helmy and El Mahallawi, 2003; Johan, 2002; Pittigrew and Hattori, 2006; Ripley, 2009). Our preliminary investigation, combining the current field survey and these new observations, reveals that the petrological and mineralogical features of the Xiadong mafic–ultramafic complex are comparable to that of an Ural–Alaskan type complex (Su et al., 2012c).

Ural–Alaskan type complexes are clearly associated with subduction in places like Alaska, so if we find them elsewhere, they must also be associated with subduction and arc magmatism. Several studies have revealed that Ural–Alaskan type intrusions are marked by extremely low abundances of some incompatible elements such as REE, low HFSE such as Nb and Zr, and relatively high LILE (e.g., Rb, Ba, Th and Sr) (Batanova et al., 2005; Eyuboglu et al., 2010; Helmy and El Mahallawi, 2003; Ishiwatari and Ichiyama, 2004; Pittigrew and Hattori, 2006; Thakurta et al., 2008). Farahat and Helmy (2006) suggested the formation of Ural–Alaskan type complexes by fractional crystallization from a common hydrous parental magma without significant crustal contamination. The positive Eu anomaly in some samples from the main body of the Xiadong complex (Fig. 8A) is consistent with their cumulate textures and suggests insignificant crustal contamination.

The Xiadong mafic–ultramafic rocks are characterized by generally low incompatible element abundances, although with large variations (Table 3S). All the rocks display identical flat REE patterns, enrichments in LILE relative to HFSE, and positive anomalies in Pb, Sr, U and Ba, and negative Nb, Ta and Zr anomalies (Fig. 8). Isotopically, the whole-rock Sr–Nd variations, especially the one clinopyroxene hornblendite with the unusually high $^{87}Sr/^{86}Sr$ ratio, indicate an oceanic alteration trend (Fig. 9), and zircon Hf–O variations (Fig. 10), further demonstrating conspicuous subduction-modified signatures in the mantle source of the Xiadong complex, as discussed in detail in the subsequent section. The zircon U–Pb ages (479 Ma, 477 Ma, 379 Ma and 313 Ma), representing the Xiadong magmatism, are consistent with the broad consensus that the subduction was continuous in the Central Tianshan during this period (Geng et al., 2009, 2011; Li et al., 2006; Su et al., 2011a, b, c, 2012a, 2013a; Xiao et al., 2004, 2009, 2010; Zhang et al., 2008). These characteristics of the Xiadong complex are akin to that of typical Ural–Alaskan type intrusions.

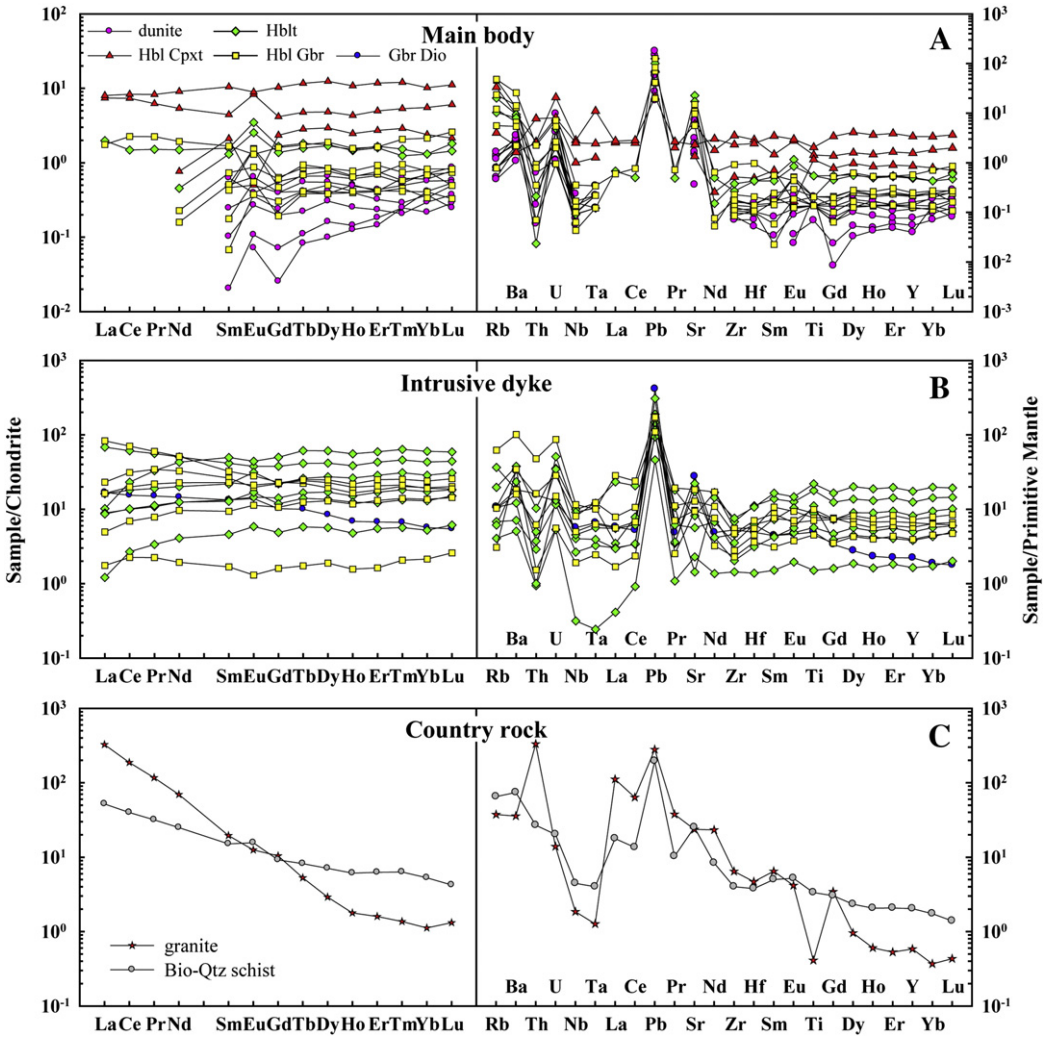

Fig. 8. Chondrite-normalized rare earth element and primitive mantle-normalized trace element patterns of the investigated rocks from the Xiadong mafic–ultramafic complex and its country rocks.
Chondrite and primitive mantle values are from Anders and Grevesse (1989) and Sun and McDonough (1989), respectively.

6.2. Mantle source

Studies have shown that mantle-derived magmas could be contaminated by crustal materials either along their ascending conduit, or by their source being contaminated before it melts (Reiners et al., 1996). The trace element abundances and patterns are useful proxies to evaluate the extent of crustal contamination (Rollinson, 1993). For example, the presence of negative Eu anomalies and REE fractionation could be related to crustal assimilation or a subducted component in mantle-derived magmas (Batanova et al., 2005; Burg et al., 2009; Reiners et al., 1996; Zhou et al., 2009). The Si-, Al- and trace element-enrichments (Table 3S), and distinct REE and trace element patterns (Fig. 8) of the granite and biotite–quartz schist are inconsistent with contamination from the country rocks during emplacement of the Xiadong complex. The extremely Mg-rich and trace element depleted signatures in most samples and the identical flat REE patterns (Fig. 8) further indicate that crustal assimilation did not significantly modify the geochemical compositions of the parental magmas of the Xiadong complex. The scarcity of orthopyroxene in Ural–Alaskan type complex also suggests that crustal contamination of the parental magma is insignificant (Farahat and Helmy, 2006). Evidence for a lack of crustal contamination is also provided by the narrow Nd isotopic range (Table 1). Consequently, the Sr–Nd–Hf–O isotopes of the mafic–ultramafic complexes can be used to trace their mantle sources and magmatic processes.

Whole-rock Nd and zircon Hf isotopes are usually used to assess the primary nature of the mantle source (Rollinson, 1993; Wu et al., 2007), whereas Sr and O isotopes are indicators of mantle metasomatism or modification (Chazot et al., 1997; James, 1981; Valley et al., 1998). The positive $\varepsilon_{Nd}(t)$ values of the Xiadong mafic–ultramafic rocks are identical to the depleted mantle member (Fig. 9). The zircon Hf isotopic values of the Xiadong complex mostly plot in the field bordered by the depleted mantle and chondrite evolution lines (Fig. 10). Thus, the parental magmas of the Xiadong mafic–ultramafic complex are inferred to have come from a depleted mantle source. On the other hand, the large Sr isotopic variation points to an oceanic trend, which has been widely interpreted as a subduction signature (e.g., Rollinson, 1993; Zindler and Hart, 1986). Such subduction-related material component could significantly increase $\delta^{18}O$ value from the normal mantle (~5.3‰) (Chazot et al., 1997; Valley et al., 1998; Zheng et al., 2004). The heterogeneous and slightly high $\delta^{18}O$ values relative to the normal mantle value (Table 2S; Fig. 10) could be ascribed to variable mantle metasomatism by subduction-related melt in the mantle source, which is consistent with the enrichment trend revealed by the Hf isotopic compositions (Fig. 10). In addition, mafic arc magmas are commonly hydrous and oxidized (e.g., Ahmed et al., 2008; Claeson and Meurer,

Table 1
Rb–Sr and Sm–Nd isotopic bulk-rock compositions of the Xiadong mafic–ultramafic complex.

Sample	Rock type	Age (Ma)	Rb (ppm)	Sr (ppm)	$^{87}Rb/^{86}Sr$	$^{87}Sr/^{86}Sr$	2σ	$(^{87}Sr/^{86}Sr)_i$	Sm (ppm)	Nd (ppm)	$^{147}Sm/^{144}Nd$	$^{143}Nd/^{144}Nd$	2σ	$(^{143}Nd/^{144}Nd)_i$	$\varepsilon_{Nd}(t)$
Main body															
XDE2	Hbl Gbr	480	0.37	410	0.003	0.705028	0.000008	0.705010	0.06	0.22	0.1658	0.512960	0.000007	0.512444	8.17
XDE3	Hbl Gbr	480	30.5	250	0.354	0.706267	0.000007	0.703882	0.26	1.12	0.1399	0.512880	0.000016	0.512445	8.18
XDE4	Hbl Gbr	480	13.4	125	0.310	0.706327	0.000007	0.704237	0.10	0.35	0.1747	0.512920	0.000006	0.512376	6.84
09XDTC1-10	Hbl Cpxt	480	2.28	45.8	0.144	0.709479	0.000010	0.708508	1.27	3.52	0.2181	0.512946	0.000006	0.512268	4.72
09XDTC1-40	Hbl Cpxt	480	0.40	26.7	0.044	0.710780	0.000013	0.710486	0.23	0.49	0.2835	0.512923	0.000007	0.512041	0.29
Intrusive body															
09XDTC1-8	Hbl Gbr	380	6.26	288	0.063	0.707306	0.000008	0.706967	3.72	14.0	0.1613	0.512774	0.000004	0.512373	4.38
09XDTC1-12	Hbl Gbr	380	6.59	215	0.089	0.706029	0.000011	0.705550	3.13	9.50	0.1995	0.512958	0.000006	0.512462	6.11
09XDTC1-22	Hbl Gbr	313	2.00	210	0.028	0.705073	0.000007	0.704951	1.40	3.97	0.2131	0.513002	0.000005	0.512565	6.45
09XDTC1-44	Hblt	380	22.5	120	0.543	0.709653	0.000011	0.706721	2.99	8.46	0.2134	0.512966	0.00001	0.512435	5.59

2004). The hydrous nature is reflected in the dominance of hornblende and localized phlogopite in the different lithologies within the intrusions. The overall enrichment of the Fe-chromite and Cr-magnetite in Fe^{3+} (Su et al., 2012c) is an original feature attributed to the oxidized nature of arc magmas (Ahmed et al., 2008).

Therefore, we suggest that the parental magmas of the Xiadong complex were derived from a depleted mantle source which had been metasomatized by subduction-related melts/fluids. The inference is consistent with the hypothesis that worldwide Ural–Alaskan type intrusions originated from subduction-related processes (Batanova et al., 2005; Chen et al., 2009; Eyuboglu et al., 2010; Ishiwatari and Ichiyama, 2004; Thakurta et al., 2008; Tian et al., 2011). The compositional modeling using olivine compositions (Fo = 93–96) by Sun et al. (2009) yields 28 wt.% MgO content in the Xiadong parental magmas. The enrichment of Cr_2O_3 in the spinels (Su et al., 2012c; Sun et al., 2009), together with the extremely high Mg and low trace element abundances, suggests that the mantle source most likely experienced a very high-degree partial melting to generate the parental magmas of the Xiadong intrusion.

6.3. Long-lived arc magmatism

Although Ural–Alaskan type complexes have been comprehensively investigated with respect to their petrology, mineralogy, geochemistry and mineralization, geochronological study has received little attention. This lack of attention is due partly to the limited analytical facilities of the early studies, and partly to the lack of reasonable dating targets in some intrusions, both of which have subjected previous findings to continuous debate. For example, Roddick and Farrar (1972) reported a K–Ar date of 175 Ma for the formation of the Tulameen complex in British Columbia. However, in the same region, Nixon and Rublee (1987) proposed an emplacement time interval of 120 Ma to 97 Ma. During the same period, an older age of 190 Ma for the Turnagain complex was reported by Scheel et al. (2005). The view that individual Ural–Alaskan type complexes are derived from one single parental magma and should have a single formation age has been accepted by many authors (e.g., Chen et al., 2009; Farahat and Helmy, 2006; Helmy et al., 2005; Tian et al., 2011).

On the other hand, many previous studies have argued that most Ural–Alaskan type complexes were formed over a long time interval caused by a long-term, continuous subduction process (Ahmed et al., 2008; Brew and Morrell, 1983; Ishiwatari and Ichiyama, 2004; Rubin and Saleeby, 1992). For example, the Klukwan–Duke mafic–ultramafic belt is recognized to have been formed over a time interval of 118 Ma to 100 Ma (Table 2; Himmelberg and Loney, 1995; Rubin and Saleeby, 1992; Saleeby, 1992). Similarly, the Ariadnoe and Koksharovka complexes in Russia have formation ages of 159–152 Ma and 160–145 Ma, respectively (Table 2; Ishiwatari and Ichiyama, 2004), while the formation age of the Kondyor complex in Russia was inferred to be in a period of 150–83 Ma (Table 2; Orlova, 1992; Kononova et al., 1995; Pushkarev et al., 2002). Furthermore, Eyuboglu et al. (2010) also suggested that Ural–Alaskan type complexes are mainly produced by successive episodes of magma replenishment and intrusion through time.

In the Xiadong complex, field relationships have revealed cross-cutting or intrusive relationships between the lithological units (Figs. 2, 3), which have been observed in many other Ural–Alaskan type complexes such as the Duke Island (Irvine, 1974) and the Karayaşmak complexes (Eyuboglu et al., 2010). There is no gradual variation in both terms of rock type and mineral assemblage from the ultramafic to mafic units. It is worth to note that enclaves of the light yellow dunites occur in the dark green dunites (Fig. 3). The hornblende seems to have had a long crystallization history as it is present in all rock types and has a wide range of Mg# (Su et al., 2012c). Furthermore, the distinct correlations of the major oxides observed between the main body rocks and intrusive dykes (Fig. 7) suggest that the Xiadong complex was probably formed by multiple magmatic pulses rather than through fractional crystallization within a single magmatism. It is also supported by the age difference

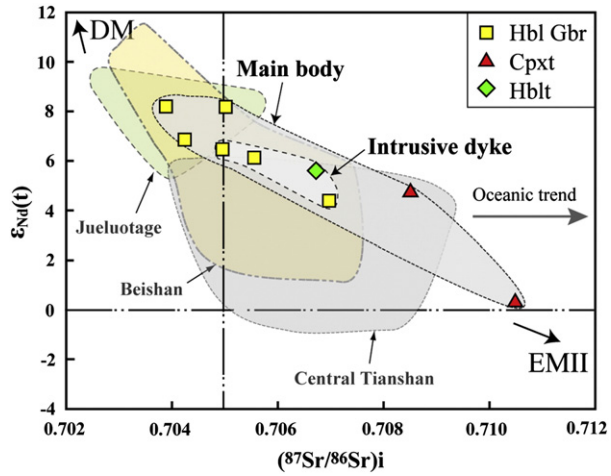

Fig. 9. $\varepsilon_{Nd(t)}$ vs. $(^{87}Sr/^{86}Sr)_i$ plot showing the Sr and Nd isotope compositions of the investigated rocks from the Xiadong mafic–ultramafic complex. All data have been adjusted to zircon U–Pb ages. The fields were defined by Nd–Sr isotopic data of mafic–ultramafic intrusions in the Jueluotage, Central Tianshan and Beishan (Su et al., 2012a and references therein). DM, depleted mantle; EMII, enriched mantle II; $\varepsilon_{Nd(t)} = 0$ and $(^{87}Sr/^{86}Sr)_i = 0.705$ are values of bulk silicate Earth (Zindler and Hart, 1986).

and changes of mantle source related to two subsequent subduction events discussed below.

The hornblende gabbro sample XED-5 has a zircon U–Pb age of 479 Ma, which is similar to the 477 Ma obtained from the borehole sample XDZK1601–20 (Fig. 6). The main body of the Xiadong complex is thus speculated to have been formed during the ~479 Ma magmatic pulse. Notably, although there should be at least two magmatic pulses to form the dunites, it is difficult to establish the exact ages due to a lack of reliable data for dating. The hornblende gabbro and hornblendite intrusive dykes in the dunite body show identical petrological and mineralogical features to those of the main body, and also to typical Ural–Alaskan type rocks (Su et al., 2012c), indicating their association with the whole Xiadong Ural–Alaskan type complex. Interestingly, two hornblende gabbro samples (09XDTC1-12 and 09XDTC1-22) from the intrusive dykes have ages of 379 Ma and 313 Ma, respectively (Table 1S; Fig. 6). Based on these data we conclude that the formation of the Xiadong Ural–Alaskan type complex lasted ~160 Ma, from 479 Ma to 313 Ma, and required extremely long-lived magmatism relative to the other Ural–Alaskan type complexes worldwide.

6.4. Tectonic implications

In the Paleozoic, the subduction of the South Tianshan and Junggar oceans as parts of the Paleo-Asian ocean resulted in an arc–basin–microcontinent system in the southern CAOB (Gao et al., 2006; Qin et al., 2003; Sengör et al., 1993; Windley et al., 2007; Xiao et al., 2009). On the other hand, the Eastern Tianshan system consists of the Dananhu–Tousuquan island arc, the Yamansu back-arc basin and the Central Tianshan microcontinent (Qin et al., 2002; Su et al., 2012a). The Dananhu–Tousuquan island arc is distinguished by Devonian and Early Carboniferous andesites and Tuwu–Yandong porphyry copper deposits (334 Ma; Han et al., 2010; Zhang et al., 2008), while the Yamansu back-arc basin is characterized by wide distributions of Carboniferous calc-alkaline volcanics, granitoids and many Fe–Cu deposits in volcanic rocks (Qin et al., 2002, 2003; Su et al., 2012a). The controversy surrounding the Central Tianshan lies in whether it originated in an island arc or continental arc setting (Li et al., 2006; Qin et al., 2002; Su et al., 2011c, 2012a; Xiao et al., 2004, 2009). Based on the discovery of a widespread Precambrian basement, the Central Tianshan has been identified as a microcontinent (Xu et al., 2009), and geochemical and geological evidence indicate that the Xiadong mafic–ultramafic complex as a Paleozoic Ural–Alaskan type formed an arc setting within the Central Tianshan.

The northward subduction of the South Tianshan Ocean in the early Paleozoic resulted in a subduction signature of the mantle source of the

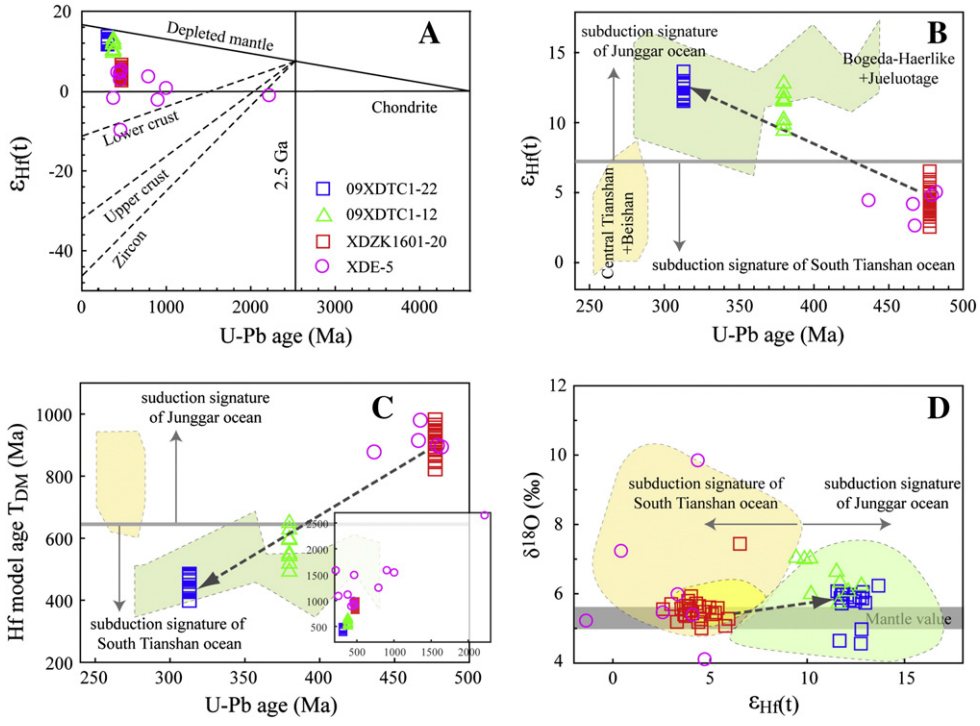

Fig. 10. Correlation diagrams of zircon Hf–O isotopes and Hf model ages vs. U–Pb ages of the Xiadong mafic–ultramafic complex. The fields were defined by zircon Hf–O isotopic data of mafic–ultramafic intrusions in the Jueluotage, Central Tianshan and Beishan (Su et al., 2011a, c). The dashed line with arrow represents the compositional variations of zircons with ages. The subduction signatures of the South Tianshan and Junggar oceans are discussed in the main text. The mantle zircon O isotopic composition of $\delta^{18}O = 5.3 \pm 0.3‰$ is from Valley et al. (1998).

Table 2
Summarized age data of representative Ural–Alaskan type complexes on the Earth.

Location	Complex	Age (Ma)	Rock/mineral	Method	Reference
Alaska, USA	Duke Island	108–111	Zircon in gabbro	U–Pb	Saleeby (1992)
		118.5	Hornblende	Ar–Ar	Meen et al. (1991)
		226	Zircon	U–Pb	Gehrels et al. (1987)
	Union Bay	102	Zircon in gabbro	U–Pb	Rubin and Saleeby (1992)
	Salt Chuck	429	Zircon in gabbro	U–Pb	Loney et al. (1987)
	Dall Island	400	Zircon in gabbro	U–Pb	Loney and Himmelberg, 1992
	Sukkwan Island	441	Zircon in gabbro	U–Pb	Loney and Himmelberg, 1992
Russia	Kondyor	149–137	Phlogopite in dunite	K–Ar	Kononova et al. (1995); Orlova (1992)
		124–113	Phlogopite in pyroxenite	K–Ar	
		120–83	Whole rock, feldspar, mica and amphibole in gabbro	K–Ar	
		132	Ultramafic rock	K–Ar	Pushkarev et al. (2002)
		115	Gabbro	K–Ar	
		123	Pyroxenite	Rb–Sr	
		340–355	Whole rock	Re–Os	Malitch and Thalhammer (2002)
	Ariadnoe	152–159	Biotite and kaersutite in pyroxenite	K–Ar	Ishiwatari and Ichiyama (2004)
	Koksharovka	145–160	Biotite and kaersutite in pyroxenite	K–Ar	Ishiwatari and Ichiyama (2004)
British Columbia	Tulameen	97–120	Biotite and kaersutite in pyroxenite	K–Ar, Rb–Sr, and U–Pb	Nixon and Rublee (1987)
China	Xiadong	313–479	Zircon in gabbro	U–Pb	This study

Early Permian mafic–ultramafic intrusions in the Beishan and Central Tianshan (Pirajno et al., 2008; Song et al., 2011; Su et al., 2011a, b, 2012a, d; Tang et al., 2011). These intrusions have features of depleted and varying whole-rock Sr–Nd isotopic ratios, slightly depleted zircon $\varepsilon_{Hf}(t)$ values (0–8), old model ages (900–600 Ma) and higher $\delta^{18}O$ values relative to the normal mantle (Figs. 9, 10; Qin et al., 2011; Song et al., 2011; Su et al., 2011a, b, 2012a, 2013b; Tang et al., 2012). On the other hand, the lithospheric mantle beneath the Eastern Tianshan is also said to have been modified by the southward subduction of the Junggar ocean (Mao et al., 2008; Zhou et al., 2004), as evidenced by the Paleozoic mafic–ultramafic intrusions in the Jueluotage, which are characterized by highly depleted and restricted Sr–Nd isotopic compositions, higher zircon $\varepsilon_{Hf}(t)$ values, and younger model ages and narrow $\delta^{18}O$ range that is close to the normal mantle (Figs. 9, 10; Qin et al., 2011; Su et al., 2011a, 2012a, 2013b).

The ~480 Ma rocks of the Xiadong complex overlap the Sr–Nd isotopic field defined by the Permian mafic–ultramafic intrusions in the Beishan Terrane (Fig. 9). Their zircons display $\varepsilon_{Hf}(t)$ values and model ages very similar to those from the Central Tianshan and Beishan intrusions. In particular, the O isotopic compositions completely plot within the Central Tianshan field (Fig. 10). As the intrusive rocks become younger, more subduction signatures from the Junggar ocean are recorded. The Nd isotopic compositions become more depleted and plot much closer to the Jueluotage field, although $(^{87}Sr/^{86}Sr)_i$ ratios are slightly variable (Fig. 9). Similarly, the Hf–O isotopes and model ages of older zircons are close to, or overlap with, the Central Tianshan and Beishan field, while the younger zircons are inside the Jueluotage field (Fig. 10). These compositional variations with time mark the transformation of subduction influences on the mantle source of the Xiadong mafic–ultramafic complex, from the South Tianshan Ocean to the Junggar ocean (Fig. 11). Therefore, it is reasonable to infer that these two successive subduction events are very significant tectonic scenarios that occurred in the southern CAOB, resulting in long-lived magmatism, variable mineralization and tectonic transformation (Fig. 11).

7. Conclusions

1) The Xiadong mafic–ultramafic complex in the Central Tianshan Terrane is characterized by high Mg, low incompatible trace element abundances, flat REE and arc–magma-type trace element patterns, which provide further constraints on the Xiadong complex as Ural–Alaskan type.
2) The cross-cutting relationship of the rock units and lack of uniform major-element correlations indicate that the Xiadong complex was formed by multiple magmatic pulses. The zircon U–Pb ages (479, 477, 379 and 313 Ma) of four hornblende gabbros confirm an extremely large time interval from Ordovician to Carboniferous, during which the Central Tianshan was inferred to be a continental arc.
3) The constant $\varepsilon_{Nd}(t)$ values, variable initial Sr isotopic ratios and zircon Hf–O isotopes, together with the abundance of hornblende and high-Fo olivine with ilmenite and magnetite, demonstrate that the parental magmas of the Xiadong complex are hydrous and oxidized, and most likely derived from a depleted mantle source through high-degree melting. Thus, the mantle source had earlier been metasomatized by melts/fluids twice, most likely from the subduction of the South Tianshan Ocean and the subduction of the Junggar ocean.

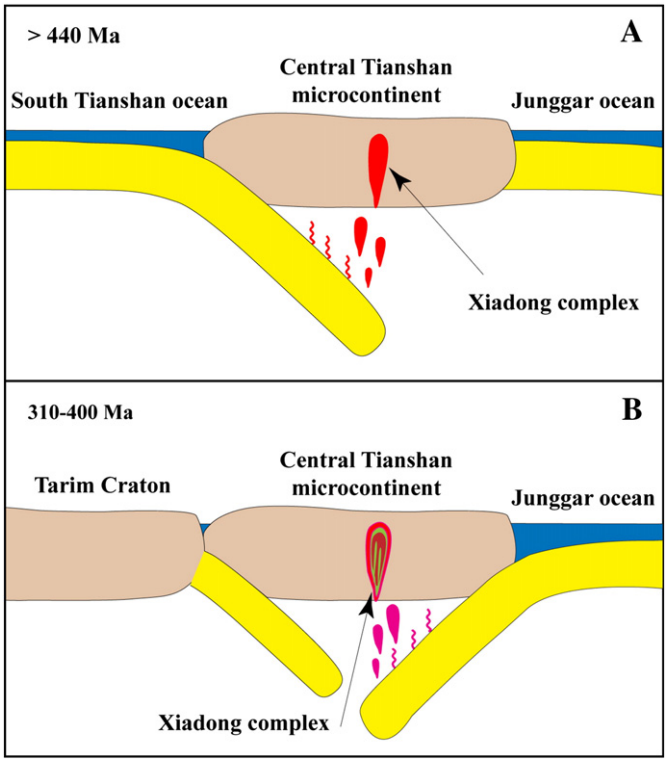

Fig. 11. Tectonic model for the formation of the Xiadong Ural–Alaskan type complex and evolution for the southern Central Asian Orogenic Belt.

Supplementary data to this article can be found online at http://dx.doi.org/10.1016/j.lithos.2014.05.005.

Acknowledgment

We are grateful to Yener Eyuboglu and an anonymous referee for providing constructive comments. We thank the editor, Prof. Nelson Eby, for his editorial handling. Aaron Brewer is acknowledged for his improving the original version of the paper. This study was financially supported by the National Natural Science Foundation of China (grants 41030424), the Opening Foundation of State Key Laboratory of Continental Dynamics, Northwest University (10LCD 05), the Foundation for the Supervisor of Beijing Excellent Doctoral Dissertation (grant 20128000101), and the Hong Kong Scholars Program (no. XJ2012048).

References

Ahmed, A.H., Helmy, H.M., Arai, S., Yoshikawa, M., 2008. Magmatic unmixing in spinel from late Precambrian concentrically-zoned mafic–ultramafic intrusions, Eastern Desert, Egypt. Lithos 104, 85–98.

Anders, E., Grevesse, N., 1989. Abundances of the elements: meteoritic and solar. Geochimica et Cosmochimica Acta 53, 197–214.

Ao, S.J., Xiao, W.J., Han, C.M., Mao, Q.G., Zhang, J.E., 2010. Geochronology and geochemistry of Early Permian mafic–ultramafic complexes in the Beishan area, Xinjiang, NW China: implications for late Paleozoic tectonic evolution of the southern Altaids. Gondwana Research 18, 466–478.

Batanova, V.G., Pertsev, A.N., Kamenetsky, V.S., Ariskin, A.A., Mochalov, A.G., Sobolev, A.V., 2005. Crustal evolution of island arc ultramafic magma: Galmoenan pyroxenites–dunite plutonic complex, Koryak Highland (Far East Russia). Journal of Petrology 46, 1345–1366.

BGMRXUAR (Bureau of Geology and Mineral Resources of Xinjiang Uygur Autonomous Region), 1993. Regional Geology of Xinjiang Uygur Autonomous Region. Geological Publishing House pp. 1–841 (in Chinese).

Brew, D.A., Morrell, R.P., 1983. Intrusive rocks and plutonic belts of southeastern Alaska, U.S.A. In: Roddick, J.A. (Ed.), Circum-Pacific plutonic terranes. Geological Society of America Memorials, 159, pp. 171–193.

Brugmann, G.E., Reischmann, T., Naldrett, A.J., Sutcliffe, R.H., 1997. Roots of an Archean volcanic arc complex: the Lac des Iles area in Ontario, Canada. Precambrian Research 81, 223–239.

Burg, J.P., Bodinier, J.L., Gerya, T., Bedini, R.M., Boudier, F., Dautria, J.M., Prikhodko, V., Efimov, A., Pupier, E., Balanec, J.L., 2009. Translithospheric mantle diapirism: geological evidence and numerical modelling of the Kondyor zoned ultramafic complex (Russian Far-East). Journal of Petrology 50, 289–321.

Chai, F.M., Zhang, Z.C., Mao, J.W., Dong, L.H., Zhang, Z.H., Wu, H., 2008. Geology, petrology and geochemistry of the Baishiquan Ni–Cu-bearing mafic–ultramafic intrusions in Xinjiang, NW China: implications for tectonics and genesis of ores. Journal of Asian Earth Sciences 32, 218–235.

Chazot, G., Lowry, D., Menzies, M., Mattey, D., 1997. Oxygen isotopic composition of hydrous and anhydrous mantle peridotites. Geochimica et Cosmochimica Acta 61, 161–169.

Chen, B., Suzuki, K., Tian, W., Jahn, B.M., Ireland, T., 2009. Geochemistry and Os–Nd–Sr isotopes of the Gaositai Alaskan-type ultramafic complex from the northern North China craton: implications for mantle–crust interaction. Contributions to Mineralogy and Petrology 158, 683–702.

Chu, Z.Y., Wu, F.Y., Walker, R.J., Rudnick, R.L., Pitcher, L., Puchtel, I.S., Yang, Y.H., Wilde, S.A., 2009. Temporal evolution of the lithospheric mantle beneath the eastern North China Craton. Journal of Petrology 50, 1857–1898.

Claeson, D.T., Meurer, W.P., 2004. Fractional crystallization of hydrous basaltic "arc-type" magmas and the formation of amphibole-bearing gabbroic cumulates. Contributions to Mineralogy and Petrology 147, 288–304.

Debari, S.M., Coleman, R.G., 1989. Examination of the deep levels of an island arc: evidence from the Tonsina ultramafic–mafic assemblage, Tonsina, Alaska. Journal of Geophysical Research 94, 4373–4391.

Eyuboglu, Y., Dilek, Y., Bozkurt, E., Bektas, O., Rojay, B., Sen, C., 2010. Structure and geochemistry of an Alaskan-type ultramafic–mafic complex in the Eastern Pontides, NE Turkey. Gondwana Research 18, 230–252.

Farahat, E.S., Helmy, H.M., 2006. Abu Hamamid Neoproterozoic Alaskan-type complex, south Eastern Desert, Egypt. Journal of African Earth Sciences 45, 187–197.

Gao, J., Long, L.L., Qian, Q., Huang, D.Z., Su, W., Klemd, R., 2006. South Tianshan: a late Paleozoic or a Triassic orogen. Acta Petrologica Sinica 22, 1049–1061 (in Chinese with English abstract).

Gao, J., Long, L.L., Klemd, R., Qian, Q., Liu, D.Y., Xiong, X.M., Su, W., Liu, W., Wang, Y.T., Yang, F.Q., 2009. Tectonic evolution of the South Tianshan orogen and adjacent regions, NW China: geochemical and age constraints of granitoid rocks. International Journal of Earth Sciences 98, 1221–1238.

Gehrels, G.E., Saleeby, J.B., Berg, H.C., 1987. Geology of Annette, Gravina, and Duke Islands, southeastern Alaska. Canadian Journal of Earth Sciences 24, 866–881.

Geng, H.Y., Sun, M., Yuan, C., Xiao, W.J., Xian, W.S., Zhao, G.C., Zhang, L.F., Wong, K., Wu, F. Y., 2009. Geochemical, Sr–Nd and zircon U–Pb–Hf isotopic studies of Late Carboniferous magmatism in the West Junggar, Xinjiang: implications for ridge subduction? Chemical Geology 266, 373–398.

Geng, H.Y., Sun, M., Yuan, C., Zhao, G.C., Xiao, W.J., 2011. Geochemical and geochronological study of early Carboniferous volcanic rocks from the West Junggar: petrogenesis and tectonic implications. Journal of Asian Earth Sciences 42, 854–866.

Han, C.M., Xiao, W.J., Zhao, G.C., Ao, S.J., Zhang, J.E., Qu, W.J., Du, A.D., 2010. In-situ U–Pb, Hf and Re–Os isotopic analyses of the Xiangshan Ni–Cu–Co deposit in Eastern Tianshan (Xinjiang), Central Asia Orogenic Belt: constraints on the timing and genesis of the mineralization. Lithos 120, 547–562.

Hattori, K., Cabri, L.J., 1992. Origin of platinum-group-mineral nuggets inferred from an osmium-isotope study. Canadian Mineralogist 30, 289–301.

Helmy, H.M., El Mahallawi, M.M., 2003. Gabbro Akarem mafic–ultramafic complex, Eastern Desert, Egypt: a late Precambrian analogue of Alaskan-type Complexes. Mineralogy and Petrology 77, 85–108.

Helmy, H.M., Ahmed, A.H., Kagami, A., Arai, S., 2005. Sm/Nd and platinum-group element geochemistry of a late-Precambrian Alaskan-type complex from the Eastern Desert of Egypt. 10th International Platinum Symposium (Abstract), Oulu, Finland, pp. 101–104.

Himmelberg, G.R., Loney, R.A., 1995. Characteristics and petrogenesis of Alaskan-type ultramafic–mafic intrusions, Southeastern Alaska. United States Geological Survey Professional Paper 1564, 1–47.

Hu, A.Q., Jahn, B.M., Zhang, G., Chen, Y., Zhang, Q., 2000. Crustal evolution and Phanerozoic crustal growth in northern Xinjiang: Nd isotope evidence 1. Isotopic characterization of basement rocks. Tectonophysics 328, 15–51.

Irvine, T.N., 1974. Petrology of the Duke Island ultramafic complex southern Alaska. Geological Society of American Memoir 138, 240.

Ishiwatari, A., Ichiyama, Y., 2004. Alaskan-type plutons and ultramafic lavas in Far East Russia, Northeast China, and Japan. International Geology Review 46, 316–331.

Jahn, B.M., Wu, F.Y., Chen, B., 2000. Massive granitoid generation in Central Asia: Nd isotope evidence and implication for continental growth in the Phanerozoic. Episodes 23, 82–92.

Jahn, B.M., Windley, B., Natal'in, B., Dobretsov, N., 2004. Phanerozoic continental growth in Central Asia. Journal of Asian Earth Sciences 23, 599–603.

James, D.E., 1981. The combined use of oxygen and radiogenic isotopes as indicators of crustal contamination. Annual Review of Earth and Planetary Sciences 9, 311–344.

Johan, Z., 2002. Alaskan-type complexes and their platinum-group element mineralization. In: Cabri, L.J. (Ed.), Geology, geochemistry, mineralogy and mineral beneficiation of platinum-group elements. Canadian Institute of Mining, Metallurgy and Petroleum, pp. 669–719.

Kononova, V.A., Pervov, V.A., Bogatikov, O.A., Mus-Shumacher, U., Keller, I., 1995. Mesozoic potassic magmatism of the Central Aldan: Geodynamics and genesis. Geotectonics 29, 224–234.

Li, J.Y., Song, B., Wang, K.Z., Li, Y.P., Sun, G.H., Qi, D.Y., 2006. Permian mafic–ultramafic complexes on the southern margin of the Tu–Ha Basin, east Tianshan Mountains: geological records of vertical crustal growth in central Asia. Acta Geoscientica Sinica 27, 424–446 (in Chinese with English abstract).

Li, X.H., Liu, Y., Li, Q.L., Guo, C.H., Chamberlain, K.R., 2009. Precise determination of Phanerozoic zircon Pb/Pb age by multi-collector SIMS without external standardization. Geochemistry, Geophysics, Geosystems 10, Q04010. http://dx.doi.org/10.1029/2009GC002400.

Li, X.H., Li, W.X., Li, Q.L., Wang, X.C., Liu, Y., Yang, Y.H., 2010. Petrogenesis and tectonic significance of the ~850 Ma Gangbian alkaline complex in South China: evidence from in situ zircon U–Pb dating, Hf–O isotopes and whole-rock geochemistry. Lithos 114, 1–15.

Loney, R.A., Himmelberg, G.R., 1992. Petrogenesis of the Pd-rich intrusion at Salt Chuck. Prince of Wales Island: an early Paleozoic Alaskan-type ultramafic body: Canadian Mineralogist 30, 1005–1022.

Loney, R.A., Himmelberg, G.R., Shew, Nora, 1987. Salt Chuck palladium-bearing ultramafic body, Prince of Wales Island. In: Hamilton, T.D., Galloway, J.P. (Eds.), Geologic studies in Alaska by the U.S. Geological Survey during 1986: U.S. Geological Survey Circular, 998, pp. 126–127.

Ludwig, K.R., 2001. Users' manual for Isoplot/Ex rev. 2.49. Berkeley Geochronology Centre Special, Publication. No. 1a p. 56.

Malitch, K.N., Thalhammer, O.A., 2002. Pt–Fe nuggets derived from clinopyroxenite–dunite massifs, Russia: a structural, compositional and osmium-isotope study. The Canadian Mineralogist 40, 395–418.

Mao, J.W., Pirajno, F., Zhang, Z.H., Chai, F.M., Wu, H., Chen, S.P., Cheng, S.L., Yang, J.M., Zhang, C.Q., 2008. A review of the Cu–Ni sulfide deposits in the Chinese Tianshan and Altay orogens (Xinjiang Autonomous Region, NW China): principal characteristics and ore-forming processes. Journal of Asian Earth Sciences 32, 184–203.

Meen, J.K., Ross, D.K., Elthon, Don., 1991. Gross isotopic heterogeneity in layered ultramafic cumulates [abs.]: EOS. Transactions of the American Geophysical Union, v. 72, p. 521.

Nixon, G.T., Rublee, V.J., 1987. Alaskan-type ultramafic rocks in British Columbia: new concepts of the structure of the Tulameen complex. B.C. Ministry of Energy, Mines and Petroleum Resources, Geologica Fieldwork pp. 281–294.

Orlova, M.P., 1992. Geology and genesis of the Konder Massif. Geology of the Pacific Ocean 8, 120–132.

Pirajno, F., Mao, J.W., Zhang, Z.C., Zhang, Z.H., Chai, F.M., 2008. The association of mafic–ultramafic intrusions and A-type magmatism in the Tianshan and Altay orogens, NW China: implications for geodynamic evolution and potential for the discovery of new ore deposits. Journal of Asian Earth Sciences 32, 165–183.

Pittigrew, N.T., Hattori, K.H., 2006. The Quetico intrusions of Western Superior Province: Neo-Archean examples of Alaskan/Ural-type mafic–ultramafic intrusions. Precambrian Research 149, 21–42.

Pushkarev, Y.D., Kostoyanov, A.I., Orlova, M.P., Bogomolov, E.S., 2002. Peculiarities of the Rb–Sr, Sm–Nd, Re–Os and K–Ar isotope systems in the Kondyor massif: mantle substratum, enriched by PGE. Regional Geology and Metallogeny 16, 80–91.

Qin, K.Z., Fang, T.H., Wang, S.L., 2002. Plate tectonics division, evolution and metallogenic settings in eastern Tianshan mountains, NW China. Xinjiang Geology 20, 302–308 (in Chinese with English abstract).
Qin, K.Z., Zhang, L.C., Xiao, W.J., Xu, X.W., Yan, Z., Mao, J.W., 2003. Overview of major Au, Cu, Ni and Fe deposits and metallogenic evolution of the eastern Tianshan Mountains, Northwestern China. In: Mao, J.W., Goldfarb, R.J., Seltmann, R., Wang, D.W., Xiao, W.J., Hart, C. (Eds.), Tectonic Evolution and Metallogeny of the Chinese Altay and Tianshan (London), pp. 227–249.
Qin, K.Z., Su, B.X., Sakyi, P.A., Tang, D.M., Li, X.H., Sun, H., Xiao, Q.H., Liu, P.P., 2011. SIMS Zircon U–Pb geochronology and Sr–Nd isotopes of Ni–Cu bearing mafic–ultramafic intrusions in Eastern Tianshan and Beishan in correlation with flood basalts in Tarim Basin (NW China): constraints on a ca. 280 Ma mantle plume. American Journal of Science 311, 237–260.
Reiners, P.W., Nelson, B.K., Nelson, S.W., 1996. Evidence for multiple mechanisms of crustal contamination of magma from compositionally zoned plutons and associated ultramafic intrusions of the Alaska range. Journal of Petrology 37, 261–292.
Ripley, E.M., 2009. Magmatic sulfide mineralization in Alaskan-type complexes. In: Li, C.S., Ripley, E.M. (Eds.), New Developments in Magmatic Ni–Cu and PGE Deposits, pp. 219–228.
Roddick, J.C., Farrar, E., 1972. Potassium–argon ages of the Eagle Grano-diorite, Southern British Columbia. Canadian Journal of Earth Sciences 9, 596–599.
Rollinson, H.R., 1993. Using Geochemical Data: Evaluation, Presentation, Interpretation. Longman Geochemistry Society, London.
Rubin, C.M., Saleeby, J.B., 1992. Tectonic history of the eastern edge of the Alexander terrane, southeast Alaska. Tectonics 11, 586–602.
Saleeby, J.B., 1992. Age and tectonic setting of the Duke Island ultramafic intrusion, southeast Alaska. Canadian Journal of Earth Sciences 29, 506–522.
Scheel, J.E., Nixon, G.T., Scoates, J.S., 2005. New observations on the geology of the Turnagain Alaskan-type ultramafic intrusive suite and associated Ni–Cu-PGE mineralization, British Columbia. British Columbia Geological Survey, Geological Fieldwork 2004. Paper 2005-1.
Sengör, A.M.C., Natal'in, B.A., Burtman, V.S., 1993. Evolution of the Altaid tectonic collage and Paleozoic crustal growth in Asia. Nature 364, 299–307.
Song, X.Y., Xie, W., Deng, Y.F., Crawford, A.J., Zheng, W.Q., Zhou, G.F., Deng, G., Cheng, S.L., Li, J., 2011. Slab break-off and the formation of Permian mafic–ultramafic intrusions in southern margin of Central Asian Orogenic Belt, Xinjiang, NW China. Lithos 127, 128–143.
Stacey, J.S., Kramers, J.D., 1975. Approximation of terrestrial lead isotope evolution by a two-stage model. Earth and Planetary Science Letters 26, 207–221.
Su, B.X., Qin, K.Z., Sakyi, P.A., Li, X.H., Yang, Y.H., Sun, H., Tang, D.M., Liu, P.P., Xiao, Q.H., Malaviarachchi, S.P.K., 2011a. U–Pb ages and Hf–O isotopes of zircons from Late Paleozoic mafic–ultramafic units in southern Central Asian Orogenic Belt: tectonic implications and evidence for an Early-Permian mantle plume. Gondwana Research 20, 516–531.
Su, B.X., Qin, K.Z., Tang, D.M., Deng, G., Xiao, Q.H., Sun, H., Lu, H.F., Dai, Y.C., 2011b. Petrological features and implications for mineralization of the Poshi mafic–ultramafic intrusion in Beishan area, Xinjiang. Acta Petrologica Sinica 27, 3627–3639 (in Chinese with English abstract).
Su, B.X., Qin, K.Z., Sakyi, P.A., Liu, P.P., Tang, D.M., Malaviarachchi, S.P.K., Xiao, Q.H., Sun, H., Dai, Y.C., Hu, Y., 2011c. Geochemistry and geochronology of acidic rocks in the Beishan region, NW China: petrogenesis and tectonic implications. Journal of Asian Earth Sciences 41, 31–43.
Su, B.X., Qin, K.Z., Sun, H., Tang, D.M., Sakyi, P.A., Chu, Z.Y., Liu, P.P., Xiao, Q.H., 2012a. Subduction-induced mantle heterogeneity beneath Eastern Tianshan and Beishan: insights from Nd–Sr–Hf–O isotopic mapping of Late Paleozoic mafic–ultramafic complexes. Lithos 134–135, 41–51.
Su, B.X., Qin, K.Z., Sakyi, P.A., Tang, D.M., Liu, P.P., Malaviarachchi, S.P.K., Xiao, Q.H., Sun, H., 2012b. Geochronologic–petrochemical studies of the Hongshishan mafic–ultramafic intrusion, Beishan area, Xinjiang (NW China): petrogenesis and tectonic implications. International Geology Review 54, 270–289.
Su, B.X., Qin, K.Z., Sakyi, P.A., Malaviarachchi, S.P.K., Liu, P.P., Tang, D.M., Xiao, Q.H., Sun, H., Ma, Y.G., Mao, Q., 2012c. Occurrence of an Alaskan-type complex in the Middle Tianshan Massif, Central Asian Orogenic Belt: inferences from petrological and mineralogical studies. International Geology Review 54, 249–269.
Su, B.X., Qin, K.Z., Sun, H., Tang, D.M., Xiao, Q.H., Liu, P.P., Sakyi, P.A., 2012d. Olivine compositional mapping of mafic–ultramafic complexes in Eastern Xinjiang (NW China): implications for mineralization and tectonic dynamics. Journal of Earth Science 23, 41–53.
Su, B.X., Qin, K.Z., Santosh, M., Sun, H., Tang, D.M., 2013a. The Early Permian mafic–ultramafic complexes in the Beishan Terrane, NW China: Alaskan-type intrusives or rift cumulates? Journal of Asian Earth Sciences 66, 175–187.
Su, B.X., Qin, K.Z., Tang, D.M., Sakyi, P.A., Liu, P.P., Sun, H., Xiao, Q.H., 2013b. Late Paleozoic mafic–ultramafic intrusions in southern Central Asian Orogenic Belt (NW China): insight into magmatic Ni–Cu sulfide mineralization in orogenic setting. Ore Geology Reviews 51, 57–73.
Sun, S.S., McDonough, W.F., 1989. Chemical and isotopic systematic of oceanic basalts: implications for mantle composition and processes. In: Saunders, A.D., Norry, M.J. (Eds.), Magmatism in the ocean basins. Geological Society Special Publication, pp. 313–345.
Sun, M., Yuan, C., Xiao, W.J., Long, X.P., Xia, X.P., Zhao, G.C., Lin, S.F., Wu, F.Y., Kröner, A., 2008. Zircon U–Pb and Hf isotopic study of gneissic rocks from the Chinese Altai: progressive accretionary history in the early to middle Palaeozoic. Chemical Geology 247, 352–383.
Sun, H., Qin, K.Z., Su, B.X., Fan, X., Tang, D.M., Li, J., 2009. Discovery of komatiitic ultramafic intrusion in Mid-Tianshan terrain: Xiadong intrusion, Xinjiang. Acta Petrologica Sinica 25, 738–748 (in Chinese with English abstract).
Tang, G.J., Wang, Q., Wyman, D.A., Li, Z.X., Zhao, Z.H., Jia, X.H., Jiang, Z.Q., 2010. Ridge subduction and crustal growth in the Central Asian Orogenic Belt: evidence from Late Carboniferous adakites and high-Mg diorites in the western Junggar region, northern Xinjiang (west China). Chemical Geology 277, 281–300.
Tang, D.M., Qin, K.Z., Li, C.S., Qi, L., Su, B.X., Qu, W.J., 2011. Zircon dating, Hf–Sr–Nd–Os isotopes and PGE geochemistry of the Tianyu sulfide-bearing mafic–ultramafic intrusion in the Central Asian Orogenic Belt, NW China. Lithos 126, 84–98.
Tang, D.M., Qin, K.Z., Sun, H., Su, B.X., Xiao, Q.H., 2012. The role of crustal contamination in the formation of Ni–Cu sulfide deposits in Eastern Tianshan, Xinjiang, Northwest China: evidence from trace element geochemistry, Re–Os, Sr–Nd, zircon Hf–O, and sulfur isotopes. Journal of Asian Earth Sciences 49, 145–160.
Taylor, H.P., 1967. The zoned ultramafic complexes of southeastern Alaska. In: Wyllie, P.J. (Ed.), Ultramafic and Related Rocks. Wiley, New York, pp. 97–121.
Thakurta, J., Ripley, E.M., Li, C.S., 2008. Geochemical constraints on the origin of sulfide mineralization in the Duke Island complex, southeastern Alaska. Geochemistry, Geophysics, Geosystems Q07003. http://dx.doi.org/10.1029/2008GC001982.
Tian, W., Chen, B., Ireland, T.R., Green, D.H., Suzuki, K., Chu, Z., 2011. Petrology and geochemistry of dunites, chromitites and mineral inclusions from the Gaositai Alaskan-type complex, North China Craton: implications for mantle source characteristics. Lithos 127, 165–175.
Valley, J.W., Kinny, P.D., Schulze, D.J., Spicuzza, M.J., 1998. Zircon megacrysts from kimberlite: oxygen isotope variability among mantle melts. Contributions to Mineralogy and Petrology 133, 1–11.
Whitehouse, M.J., Kamber, B.S., 2005. Assigning dates to thin gneissic veins in high grade metamorphic terranes: a cautionary tale from Akilia, Southwest Greenland. Journal of Petrology 46, 291–318.
Whitehouse, M.J., Kamber, B.S., Moorbath, S., 1999. Age significance of U–Th–Pb zircon data from early Archaean rocks of west Greenland—a reassessment based on combined ion-microprobe and imaging studies. Chemical Geology 160, 201–224.
Wiedenbeck, M., Hanchar, J.M., Peck, W.H., Sylvester, P., Valley, J., Whitehouse, M., Kronz, A., Morishita, Y., Nasdala, L., Fiebig, J., Franchi, I., Girard, J.P., Greenwood, R.C., Hinton, R., Kita, N., Mason, P.R.D., Norman, M., Ogasawara, M., Piccoli, R., Rhede, D., Satoh, H., Schulz-Dobrick, B., Skar, O., Spicuzza, M.J., Terada, K., Tindle, A., Togashi, S., Vennemann, T., Xie, Q., Zheng, Y.F., 2004. Further characterisation of the 91500 zircon crystal. Geostandards and Geoanalytical Research 28, 9–39.
Windley, B.F., Alexeiev, D., Xiao, W., Kroner, A., Badarch, G., 2007. Tectonic models for accretion of the Central Asian Orogenic Belt. Journal of the Geological Society of London 164, 31–47.
Wu, F.Y., Yang, Y.H., Xie, L.W., Yang, J.H., Xu, P., 2006. Hf isotopic compositions of the standard zircons and baddeleyites used in U–Pb geochronology. Chemical Geology 234, 105–126.
Wu, F.Y., Li, X.H., Zheng, Y.F., Gao, S., 2007. Lu–Hf isotopic systematics and their applications in petrology. Acta Petrologica Sinica 23, 185–220 (in Chinese with English abstract).
Xiao, W.J., Zhang, L.C., Qin, K.Z., Sun, S., Li, J.L., 2004. Paleozoic accretionary and collisional tectonics of the eastern Tianshan (China): implications for the continental growth of Central Asia. American Journal of Science 304, 370–395.
Xiao, W.J., Windley, B.F., Yuan, C., Sun, M., Han, C.M., Lin, S.F., Chen, H.L., Yan, Q.R., Liu, D.Y., Qin, K.Z., Li, J.L., Sun, S., 2009. Paleozoic multiple subduction–accretion processes of the southern Altaids. American Journal of Science 309, 221–270.
Xiao, W.J., Huang, B.C., Han, C.M., Sun, S., Li, J.L., 2010. A review of the western part of the Altaids: a key to understanding the architecture of accretionary orogens. Gondwana Research 18, 253–273.
Xu, X.Y., He, S.P., Wang, H.L., Chen, J.L., 2009. Geological Background Map of Mineralization in Eastern Tianshan–Beishan Area (in Chinese).
Zhang, H.F., Sun, M., Lu, F.X., Zhou, X.H., Zhou, M.F., Liu, Y.S., Zhang, G.H., 2001. Geochemical significance of a garnet lherzolite from the Dahongshan kimberlite, Yangtze Craton, southern China. Geochemical Journal 35, 315–331.
Zhang, L.C., Qin, K.Z., Xiao, W.J., 2008. Multiple mineralization events in the eastern Tianshan district, NW China: isotopic geochronology and geological significance. Journal of Asian Earth Sciences 32, 236–246.
Zheng, Y.F., Wu, Y.B., Chen, F.K., Gong, B., Li, L., Zhao, Z.F., 2004. Zircon U–Pb and oxygen isotope evidence for a large-scale ^{18}O depletion event in igneous rocks during the Neoproterozoic. Geochimica et Cosmochimica Acta 68, 4145–4165.
Zhou, M.F., Lesher, C.M., Yang, Z.X., Li, J.W., Sun, M., 2004. Geochemistry and petrogenesis of 270 Ma Ni–Cu-(PGE) sulfide-bearing mafic intrusions in the Huangshan district, Eastern Xinjiang, Northwest China: implications for the tectonic evolution of the Central Asian Orogenic Belt. Chemical Geology 209, 233–257.
Zhou, M.F., Zhao, J.H., Jiang, C.Y., Gao, J.F., Wang, W., Yang, S.H., 2009. OIB-like, heterogeneous mantle sources of Permian basaltic magmatism in the western Tarim Basin, NW China: implications for a possible Permian large igneous province. Lithos 113, 583–594.
Zindler, A., Hart, S.R., 1986. Chemical geodynamics. Annual Review of Earth and Planetary Sciences 14, 493–571.